2-14-2014

Model systems for the study of active phase evolution in complex bimetallic catalysts (PdZn)

Jonathan Paiz

Jonathan Andrew Paiz
Candidate

Chemical and Nuclear Engineering
Department

This dissertation is approved, and it is acceptable in quality and form for publication:

Approved by the Dissertation Committee:

Abhaya K. Datye , Chairperson

Plamen B. Atanassov

Adrian J. Brearley

Tim L. Ward

Model systems for the study of active phase evolution in complex bimetallic catalysts (PdZn)

BY

Jonathan Andrew Paiz

BS. Chemical Engineering 2009
2nd Major Spanish 2009

DISSERTATION

Submitted in Partial Fulfillment of the
Requirements for the Degree of

Doctor of Philosophy

Engineering

Minor

Nanoscience and Microsystems Engineering

The University of New Mexico
Albuquerque, New Mexico

December, 2013

DEDICATION

Para mi abuela:

Nuestra familia está aquí hoy porque es una mujer luchadora. Usted no tiene miedo a nada.

Le quiero mucho y gracias por todo.

- Jona

ACKNOWLEDGMENTS

First and foremost I would like to thank my advisor Abhaya K Datye for all his guidance and support. I would like to thank my fellow group members specifically Angelica Benavidez for providing me with my 1wt% Pd/ZnO sample that was used throughout this study and Andrew de la Riva for his assistance with the TEM. I would also like to thank Eric J. Peterson for the XRD data that he provided for me. I would like to thank Travis Conant who served as my mentor as an undergraduate student. Thanks to Tyler Hough, my undergraduate student who made the aerosol samples and thanks to Laura Crossey for her devotion to her LSAMP students and managing the Louis Stokes Minority fellowship at UNM. This fellowship provided funding for my research, tuition and living expenses for several semesters during my program. I would also like to thank Hans Niemantsverdriet, Peter Thüne and past members of the Schuit Institue of Catalysis for their guidance and advisement while I participated in the NSF Partnership for International Research and Education at the Eindhoven University of Technology in the Nederlands. My experiences during those two summers in the Nederlands were fundamental in shaping my PhD project and I am forever grateful.

Financial support for my research project was provided by the Department of Energy and the National Science Foundation Grant # *1026412*. I would like to thank Bruce Anderson, Werner Barnard, Dave Mitchell, Willem Erasmus of Sasol Technologies and Jaco Oliver of Nelson Mandela Metropolitan University for their TEM and Raman expertise and use of their equipment and facilities. I would like to thank the University of New Mexico for the use of their TEM lab and finally, I would like to thank my committee members: Dr. Atanassov, Dr. Brearley, Dr. Datye and Dr. Ward.

Model systems for the study of active phase evolution in complex bimetallic catalysts (PdZn)

BY

Jonathan Andrew Paiz

BS. Chemical Engineering 2009
2nd Major Spanish 2009

Doctor of Philosophy: Engineering
Minor: Nanoscience and Microsystems Engineering

ABSTRACT

This study used PdZn as a model system to investigate phase transformations and its influence on reactivity. Aerosol synthesis was used to study the oxide precursors of the PdZn system, spin coating was used to synthesize model PdZn nanoparticles for phase transformations studies and preliminary work with CO oxidation coupled with methanol steam reforming (MSR) was used to gain insight into *in-situ* surface reactivity of PdZn for MSR. Multiple characterization techniques including XRD, Raman Spectroscopy, XPS, EDX along with TEM and STEM were used to gain valuable insight into the nature of the samples used in these studies.

Investigations into the Pd:Zn aerosol derived oxides demonstrated the existence of 2 mixed oxides, a previously undocumented (Pd,Zn)O and a greater characterized bulk (Zn,Pd)O. TEM and SEM were used to show to distinct phases of different morphologies and EDX showed the differences in Pd and Zn ratios for each phase. XRD was used to demonstrate the change in unit cell volume of PdO and Raman was used to show incorporation of Pd into the ZnO lattice.

The model system synthesized via spin coating demonstrated a simple platform for the study of complex multimetallic catalysts. The use of the silica as a TEM support combined with aberration corrected HRSTEM, EDX, XPS and Raman allowed for a very detailed look into PdZn nanoparticle formation from (Pd,Zn)O → α-Pd → β1-PdZn → Pd_2Zn and back to α-Pd. This study provided insight into the role of reduction temperature, showing that nanoparticles of the desired tetragonal PdZn phase can be formed at relatively low temperatures on suitable supports along with phase transformations leading to changes in activity.

CO oxidation studies of 1wt% Pd/ZnO gave insight into the dynamic nature of the PdZn system at various reduction temperatures. The preliminary results suggest that the number of active sites decrease on Pd/ZnO with increase in reduction temperature while MSR activity remains constant, this implies that lager particles show higher turn over frequency for MSR.

Table of Contents

List of Figures

Chapter 1.

Introduction

1.1 Statement of Research Problem

Over 90% of the chemicals produced in the world utilize catalysts [1]. Monometallic catalysts such as Pd or Pt are excellent catalysts alone but it has been shown that adding a second metal component or promoter can drastically improve their activity [2]. Recent trends in heterogeneous catalysis have been the design of active surface sites, which have led to investigations into the effects of size and composition on the catalytic behavior of bimetallic systems [4]. Conventional methods used to synthesize bimetallic or multimetallic supported catalysts such as coimpregnation or coprecipitation may lead to particles of similar sizes however, these methods do not achieve uniformity of composition at the scale of individual nanoparticles [2]. This lack of uniformity makes it difficult to achieve the best performance since the different phases and compositions can have very different catalytic behavior [1].

Thus to engineer catalysts with unsurpassed selectivity and to understand fundamental reactivity questions; we must also achieve control over composition along with particle size, since both these parameters influence catalytic behavior [8]. The objective of my research is to develop methods that would allow synthesis of model bimetallic system with uniform phase and composition. This study will also use PdZn as a model system to investigate phase transformations and their influence on reactivity.

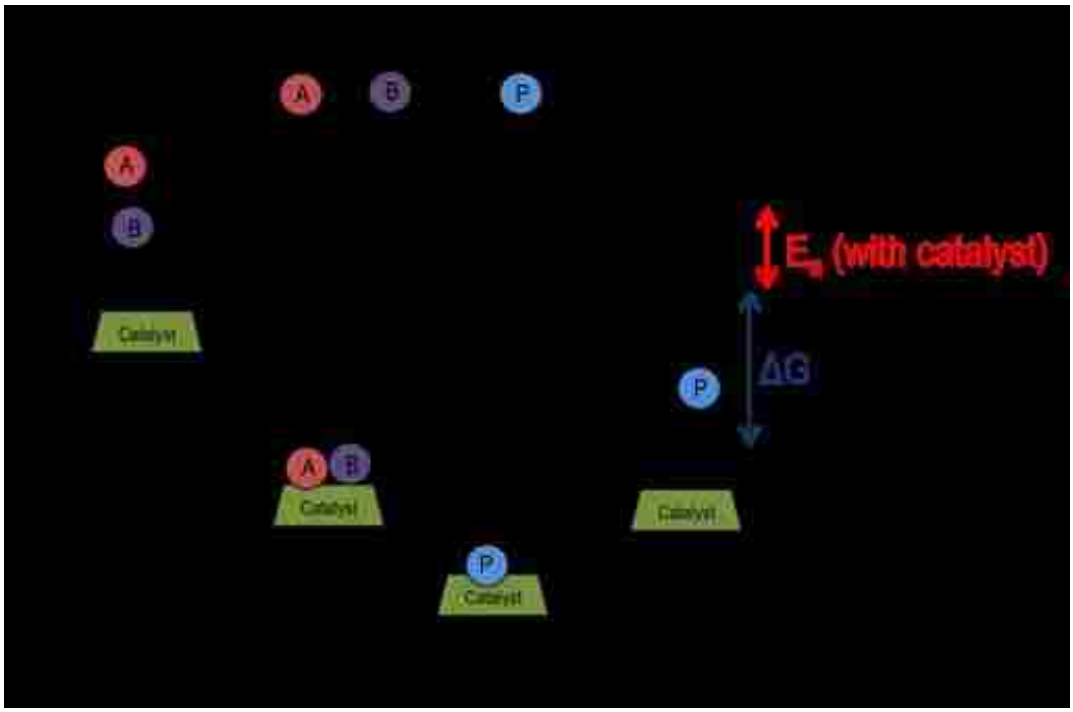

Figure 1.1 Potential Energy Diagram for catalytic and non-catalytic reaction

The PdZn system is an ideal model since the phase diagram for the system is complex, with several possible phases, not all of which have been observed in supported Pd/ZnO catalysts. Thus it would be of interest to determine conditions under which these various phases are formed using model platforms so that their reactivity can be explored.

1.2 Introduction to Catalysis

A catalyst accelerates a chemical reaction without being consumed in the process. For a specific chemical reaction with multiple outcomes, a catalyst may lead to the production of one desired product [9]. For these processes catalysts are used throughout industry for selective chemical synthesis. From the production of raw chemicals to the development of new forms of energy, catalysis is a key component of our daily lives.

A catalyst offers an alternative path for a chemical reaction usually more energetically favorable and of a higher reaction rate. Figure 1.1 is a potential energy diagram for the overall exothermic catalytic and non-catalytic reaction between reactants A and B and it illustrates many important concepts in catalysis.

For the non-catalytic reaction, the reactants simply collide and react. In order for this to take place a significant amount of energy is needed to overcome the activation energy barrier (E_a), with the change in Gibbs free energy between the products and reactants being ΔG.

In the catalytic reaction the reaction is first initiated by the adsorption of the reactants on the surface of the catalyst. Depending on the size of the first energy barrier this process can be either spontaneous or require a certain activation energy (E_a). The reaction then proceeds on the surface when the other discrete activation energy barriers are surpassed. The energy required to overcome these steps is significantly much lower than the non-catalyzed reaction forming the overall product. After an endothermic barrier, the product desorbs off the surface of the catalyst.

Since the overall free energy change (ΔG) of the uncatalyzed reaction and catalyzed reaction are the same the equilibrium constant for the reaction is not affected by the catalyst. Thus if a reaction is thermodynamically unfavorable it will not take place. The catalyst only has an affect on the kinetics, not the thermodynamics.

Understanding the active phase of a catalyst is crucial in the synthesis of highly selective and stable catalytic systems [9].

1.3 Heterogeneous Catalysis

A catalyst can either be homogenous (of the same phase as the reactants) or heterogeneous (of a different phase). A vast majority of heterogeneous catalysts are in the form of nanoparticles, which allow for a large concentration of active surface sites [9]. These nanoparticles are usually supported on high surface area oxides. In heterogeneous catalysis the reactants are in the gas or solution phase differing from the solid state of the catalyst itself. Monometallic catalysts can be highly selective alone, however it has been shown that adding a second metal component or promoter can drastically improve their activity [2].

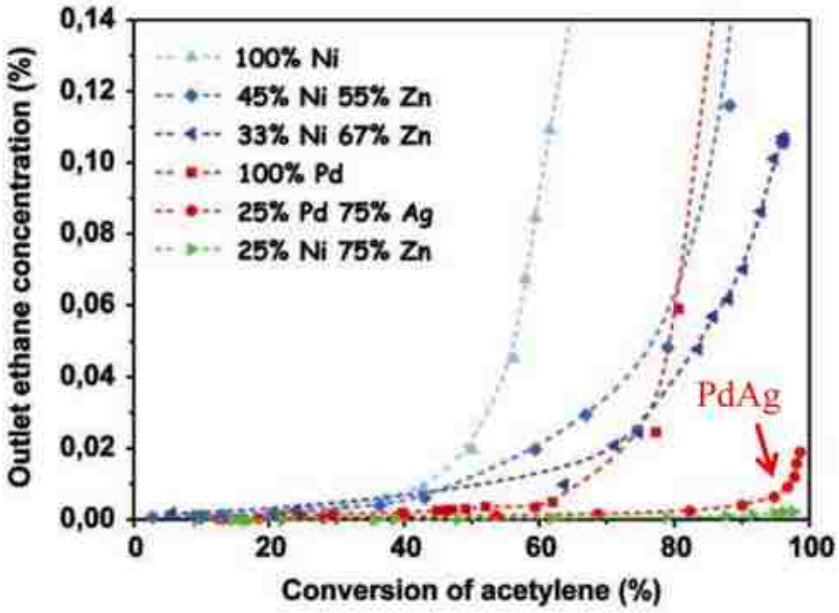

Figure 1.2 Conversion of acetylene for monometallic and bimetallic catalysts. PdAg is more selective than both Ni and Pd since it has the lower outlet ethane concentration [7].

1.4 Bimetallic Catalysts: Improved Selectivity & Surface Chemistry

An example of a reaction that is affected by the addition of a second metal is the selective hydrogenation of acetylene. Acetylene (C_2H_2) is formed as a byproduct of ethylene (C_2H_4) production:

$$C_2H_2 \rightarrow C_2H_4 \rightarrow C_2H_6 \text{ (Equation 1.1)}$$

Acetylene must be removed from the feed ethylene stream to prevent poisoning of the downstream Ziegler-Natta catalysts used to make polyethylene. Pd alone has a strong tendency to hydrogenate which leads to the formation of ethane (C_2H_6). However, the addition of Ag to Pd leads to a more selective catalyst minimizing ethane formation. Since PdAg has high conversion of acetylene, and selectivity towards ethylene, it is favored in industry (Figure 1.2) [7].

The actual effect that a second metal component has on a monometallic catalyst can be attributed to a number of electronic and structural effects. The addition of these components may lower or increase various activation energy barriers for a particular reaction pathway. Rodriguez *et al.* [10, 11] reviewed a number of studies involving flat model bimetallic surfaces. These surfaces were generated by vapor deposition of one metal onto a crystal face of a second metal. This vapor deposition technique yielded model bimetallic systems in which electronic and chemical properties could be studied on an atomic scale. These studies revealed that the addition of the second metal component causes an electronic perturbation leading to a drastic change in the chemical properties of both components. However today with the help of modeling, it is possible to screen potential metallic combinations for electronic effects, which may affect overall activity and selectivity.

1.4.1 Lack of Uniformity in Bimetallic Systems

High throughput computer based density functional theory (DFT) modeling has changed the way in which bimetallic systems for specific reactions are chosen. Selective catalysts today are chosen on atomic arrangements of alloy and intermetallic compounds modeled though complex DFT techniques [4, 9]. The difficulty however is synthesizing these unique compounds and maintaining their stability under reaction conditions. A majority of these compounds are classified either as intermetallic, which is a chemical compound of two or more metallic elements with an ordered crystal structure, or simply an alloy, which is a mixture of metals. The intermetallic compounds themselves depending on the elements can have a multitude of phases [1, 12].

For a number of systems these intermetallic compounds are formed *in-situ*. Some examples of *in-situ* active phase formation include: Pt/ZnO, for the selective hydrogenation of crotonaldehyde, which forms PtZn under reaction conditions, and Pd/ZnO, the model system mentioned previously. Pd/ZnO forms PdZn, which is active for methanol steam reforming (MSR).

Since these species are formed on stream it is difficult to understand the precursors and formation of the active species. This lack of knowledge of species formation and stability make optimization of these catalysts difficult [1, 12].

1.4.2 Bimetallic Catalyst Synthesis Methods

Further complicating the systems are synthesis methods of the catalysts themselves. Coprecipitation and coimpregnation are two techniques commonly used to synthesize supported bimetallic catalysts. Mouljin *et al.* [8] describes coprecipitation as an analogy to building and pushing over a brick wall, meaning coprecipitation is a synthesis technique that

is multistep; with the final product being very different from the initial precursors. Where impregnation involves the slow addition of a solution containing metal precursors to a support leading to the same result.

These techniques are favored in industry due to their ease of use. However when used for bimetallic systems, it is difficult to control phase and composition at the nanoscale making phase stability studies difficult. These issues are ever present for the bimetallic PdZn system. Pd supported on ZnO is an extremely active catalyst where phase transformation is essential in producing a highly stable and selective catalyst for reactions like methanol steam reforming.

1.5 PdZn and Methanol Steam Reforming (MSR)

Methanol is an attractive H_2 source for compact fuel cell systems. These fuel cell systems have been deemed as an alternative to batteries in low power portable electronics. Methanol is a viable candidate since it is sulfur free and can be reformed at low temperatures (200-250˚C) via MSR. (Equation 1.2)

$$CH_3OH + H_2O \rightarrow 3H_2 + CO_2 \quad \text{(Equation 1.2)}$$

Early studies used Cu as a catalyst for MSR due to its high selectivity to CO_2 and high yield of H_2. However, Cu as a catalyst suffered from fast deactivation due to poor thermal stability at higher temperatures and was difficult to store and maintain due to its overall pyrophoric nature [13].

Other metals like Pd tend to form CO via the decomposition of methanol (Equation 1.3).

$$CH_3OH \rightarrow 2H_2 + CO \text{ (Equation 1.3)}$$

Although methanol decomposition forms H_2 the formation of CO must be minimized since it poisons the Pt catalysts used in the PEM fuel cells. However when Zn is added to Pd it is highly selective (less than 1.5% CO in product stream) and active for MSR. Iwasa and coworkers [6] were the first to report this enhanced activity and selectivity of Pd supported on ZnO after high temperature reduction (> 300˚C) [6].

Understanding the mechanism of MSR on the surface of PdZn is essential in the design of highly selective and stable catalysts. Experimental (XPS) and theoretical (DFT) measurements have shown similarities in the valance density of states of Cu and PdZn [14]. Neither mechanism on each surface is well understood however it is known that the addition of Zn to Pd (111) inhibits methanol decomposition in the MSR reaction. Similar to the

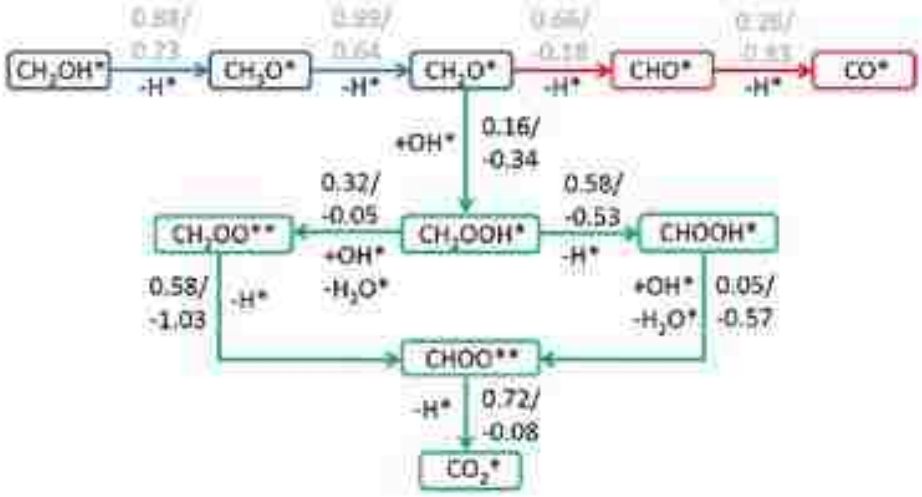

Figure 1.3 Proposed reaction network for MSR on PdZn. Reaction barriers are given in black, CO pathway red and CO_2 in green [16]

inhibition on Cu. Recently Lin [14] and coworkers have proposed that the reaction mechanism on PdZn is very similar to the mechanism on Cu. Through DFT calculations it appears that both surface have the same reaction between the formaldehyde intermediate and the surface hydroxyl species [14].

According to Lyn the closed shell species (H_2O CO_2 CHOOH) tend to weakly adsorb to PdZn(111) sites, the adsorbates however have slight preferences for Zn sites.

The proposed reaction network can be found in Figure 1.3. For both PdZn and MSR the reaction is first established by O-H bond cleavage of adsorbed methanol. The reaction is then limited by the dehydrogenation of methoxyl. After the dehydrogenation a formaldehyde intermediate is formed which immediately reacts with a surface hydroxyl produced from H_2O decomposition. Since this reaction happens quickly and with less activation energy CO is not formed. As the reaction proceeds on the surface two pathways are possible, which both lead to formate formation and ultimately CO_2 desorption. This most recent proposed mechanism of MSR is further backed by experimental data and shows the importance of the formaldehyde as an intermediate[14].

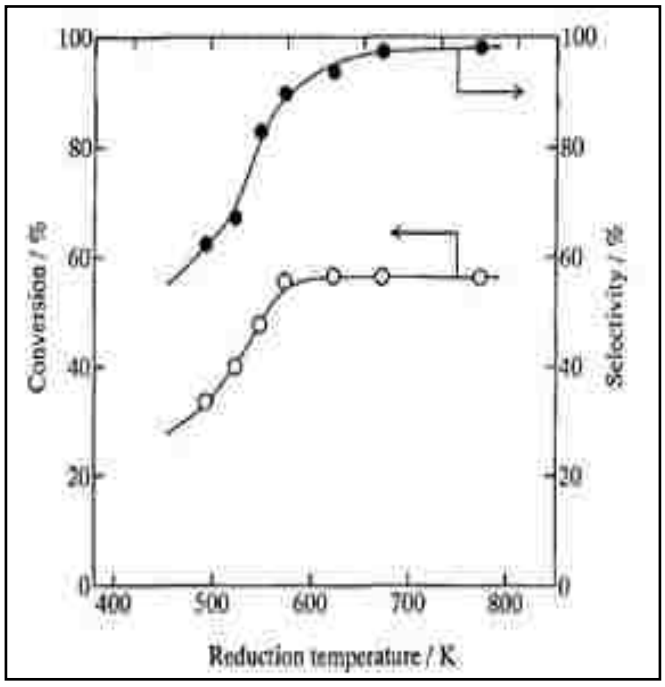

Figure 1.4 Conversation and selectivity as a function of reduction temperature for Pd/ZnO. Selectivity approaches nearly 99% at 700K (427˚C) and conversion is stable after 600K (327 ˚C) [6]

1.5.1 Effect of Reduction Temperature on Pd/ZnO for MSR

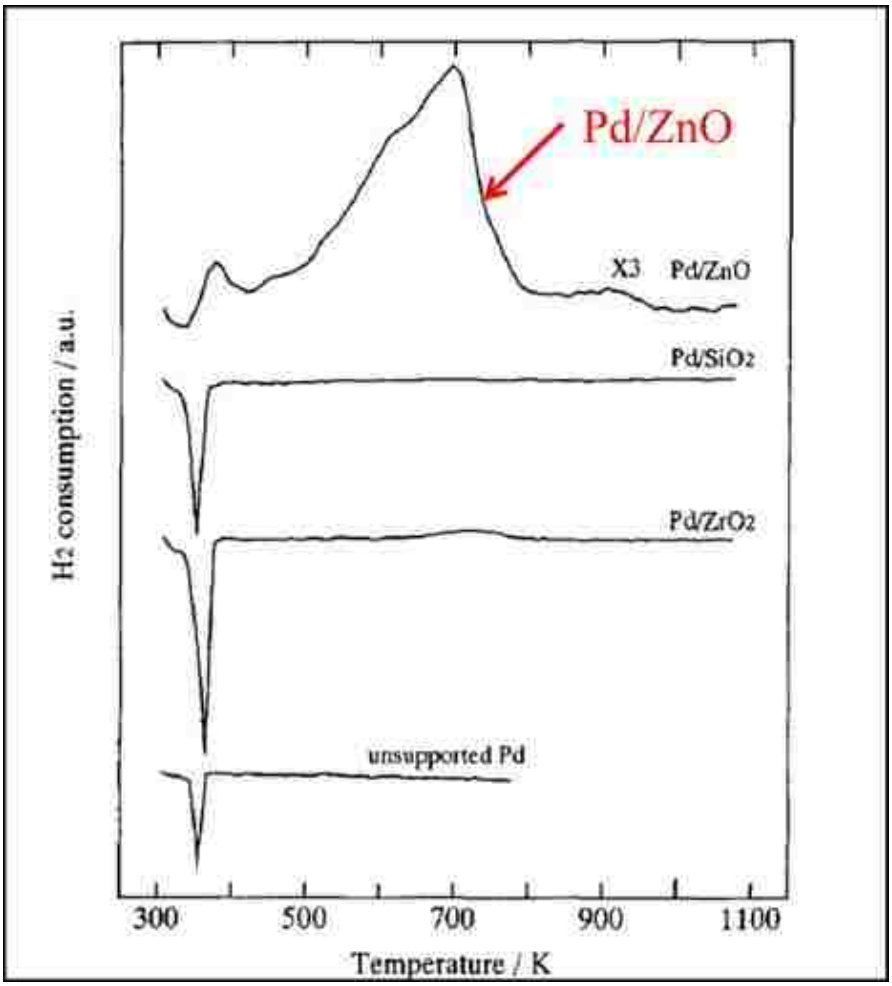

Figure 1.5 TPR profile as a function of reduction temperature (Top: Pd/ZnO) Desorption of H_2 is seen at 335K (62˚C). A broad peak corresponding to extensive phase transformation begins at 400K (127˚C) and is present until 800K (527˚C) [6]

Iwasa *et al.* [6] synthesized 10 wt% Pd/ZnO by impregnation of Pd nitrate onto powdered ZnO. The sample was packed into a conventional packed bed reactor and reduced in H_2 at 5 K/min at various temperatures. After reduction MSR was carried out. The selectivity and conversion of the Pd/ZnO sample after each specific reaction temperature is given in Figure 1.4. According to the data, the selectivity increases with the increase of reduction temperature; the conversion also increases, however it remains constant above

700K (427˚C). Temperature programmed reduction experiments showed small hydrogen consumption at room temperature for the Pd/ZnO catalysts. Desorption of hydrogen occurred at 335 K (62˚C) signified by an inverse TPR peak (Figure 1.5). Hydrogen consumption began at (420 K) 147˚C signified by a large broad peak with maximum consumption at (700 K) 427˚C with decline there after (Figure 1.4)

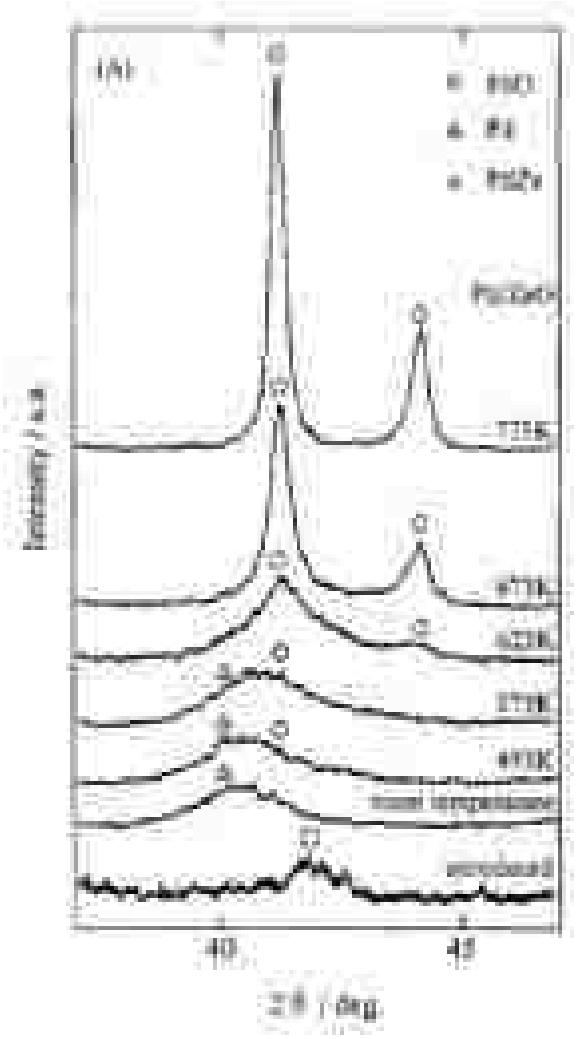

Figure 1.6 XRD profiles for increasing reduction temperatures (Pd/ZnO) [6]

XRD was also performed on the sample. The unreduced catalyst shows very broad peaks signifying the existence of PdO. As the catalyst is reduced at room temperature, broad

peaks corresponding to Pd are formed. With further increase in temperature broad PdZn peaks begin to form at 623K (350˚C). These PdZn peaks become more intense and become sharper as the reduction temperature increases further (Figure 1.6). Iwasa and coworkers [6] attributed the increased selectivity and conversion to the formation of PdZn/ZnO. Although very interesting, these studies do not tell us the nature of the active phase formation due to the extremely broad beaks formed via XRD and the large TPR peak seen from 420K (147˚C) to 800K (527˚C). The large TPR peak itself does not clearly define the temperature at the active phase transforms. A majority of the information is lost in the broad peaks from these techniques.

The authors also do not explain why the conversion levels off with the increased height of the XRD PdZn peaks. These sharp peaks correspond to an increase of PdZn crystallite size signifying a change in surface area, which must imply a change in turn over frequency (TOF) or the catalysts itself must be structure sensitive.

In heterogeneous catalysis, structure sensitivity is a change in TOF dependent on anisotropy of the metal crystal. Traditionally this effect has been limited to nanoparticles with different faces that are less than 10 nm in size [15]. However it has been shown that larger nanoparticles can posses various faces and kinks that have an affect on overall reactivity [16]. Such may be the case for the PdZn system. Large PdZn particles rarely consist of smooth faces, once large these particles tend to be non-uniform and posses many kinks and ledges. Recent DFT studies performed by Neyman and coworkers [17] have shown differences in activation energy for various mechanistic steps of MSR on PdZn. In their studies they found that surface steps which are most likely PdZn(221) planes facilitate the decomposition of CH_3O to CH_2O both kinetically and thermodynamically. These low

coordinated sites tend to favor formation of formaldehyde, which these sites may be in greater quantity in larger PdZn particles[17].

Measuring active sites for the PdZn system via traditional techniques (CO and H_2 chemisorption) is relatively difficult since the stoichiometry of CO on Pd is variable and H_2 has been known to react with Pd forming Pd hydride [18]. Understanding the change in TOF and surface sensitivity for this system is essential for characterization of the most active phase for MSR. Since Iwasa's studies, the change in TOF with treatment temperature has not yet been addressed for the supported PdZn system [13, 18-22].

1.6 Model PdZn Systems for the Study of Phase Transformation

Characterization of the active phase for various bimetallic systems including PdZn is difficult due to the oxide support. The supports act as insulators which do not allow a number of characterization techniques to be fully utilized (XPS, TEM) [5].

Model PdZn studies have been conducted to understand the fundamental phase transformations without the presence of a powdered support. These methods traditionally use flat substrates with deposited nanoparticles. Penner *et al.* [23] synthesized a model bimetallic PdZn through a UHV deposition technique. Pd metal was deposited on a freshly cleaved

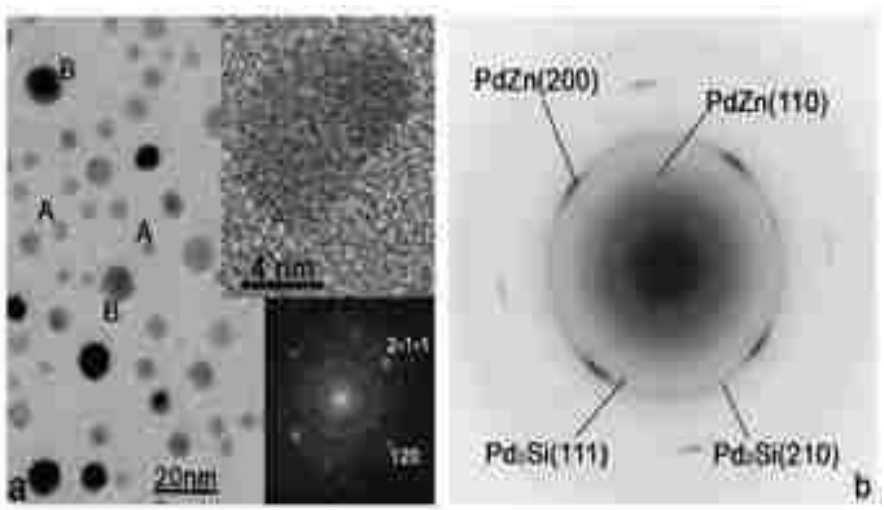

Figure 1.7 a) TEM overview of $Pd/ZnO/SiO_2$ catalyst after reduction at 600˚C b) Selected area electron diffraction pattern of sample showing existence of Pd_2Si [17]

NaCl (001) substrate. The thin film resulted in Pd nanoparticles of 5 nm in size. The newly formed Pd nanoparticles were than covered with amorphous ZnO at various atomic ratios. The amount of ZnO was confirmed using EDX, and HRTEM was used to observe the change in the morphology of the nanoparticles. The authors wanted to understand the structure and thermal stability of the PdZn system. The authors noted no noticeable change after reducing under 1bar of H_2 at temperatures below 200ºC. However, changes in morphology were found at reduction temperature above 250ºC including an increase in particle diameter. The authors found that they began to loose PdZn at temperatures above 500ºC (Figure 1.6).

Penner *et al.* [23] however did not do extensive studies into the catalysts before reduction nor did they measure the system's elemental compostion during treatment. Also, they deposited the metals via physical vapor deposition not via liquid phase routes. Industrial heterogeneous catalysts are prepared using liquid phase precursors. To mimic industrial catalysts there is a need for model systems synthesized using aqueous precursors

that can provide insight into the formation and stability of metallic nanoparticles relevant to industrial heterogeneous catalysts.

1.7 Summary

Much is still to be learned about active phase transformations for bimetallic catalysts. The PdZn system in particular is extremely complex with a number of phases, many which are not fully understood. The following are a few questions that still remain:

- The first step in the preparation of the PdZn alloy catalyst involves mixing of Pd and Zn precursors followed by calcination, what is the nature of this oxide phase?
- Multiple phases of nanoparticles can be seen on the same catalyst when liquid precursors are used; is it possible to control composition and size when using liquid precursors? Also, at what temperatures do these nanoparticles undergo phase transformations and when is uniformity lost?
- TOF is difficult to measure on PdZn, how does the TOF frequency change with PdZn phase transformations for MSR and with crystallite size?

The focus of this work is therefore to address these questions and to gain insight into the active phase transformation of the PdZn system.

1.8 Hypothesis

- Little is known about the starting oxide phase in the PdZn system. Based on the literature it is possible that the PdZn initial starting material is composed of one separate oxide phase, a combined phase of Zn, Pd and O. This phase then loses oxygen to become a uniform intermetallic when exposed to high temperature reduction. This may explain the very broad PdO peak seen by Iwasa *et al.* [6] for his as prepared Pd/ZnO.
- Current techniques of catalysts synthesis lead to lack of compositional uniformity. Spin coating can be used to control composition and particle size due to the quick evaporation of the solvent from the system. The nanoparticles themselves will initially be uniform but ultimately lose Zn through metallic Zn when exposed to high temperature reduction. This may explain the high temperature phase transformation of the PdZn particles seen by Penner *et al.* [23]. Penner believed that Pd silicides were formed at high temperatures, however it is more likely that the thermodynamically stable Pd_2Zn phase formed.
- Measuring turn over frequency for each phase transformation for the PdZn system is relatively difficult since we are unable to use chemisorption to count active sites. Therefore using CO oxidation to count active sites, one can measure TOF for the various *in-situ* phase transformations for PdZn. From Iwasa's [6] work one can assume that the TOF will change with alloy formation and increase in PdZn crystallite size.

1.9 Significance of Work

This research is applicable to all areas of catalysis that utilize bimetallics. Understanding the fundamental characteristics that affect nanoscale composition and size is essential in developing a general-purpose catalyst manufacturing technique. These new findings will also be beneficial for the PdZn system yielding a highly selective and much more stable catalyst.

Chapter 2.

Model Catalyst Approach

2.1 Model Catalytic Systems

The advances of characterization over the last century have provided essential insight into the active phases in heterogeneous catalysis. Understanding the surface in as much detail as possible has been the driving force for the development of these techniques. Although advanced, a number of these methods are limited by the true nature of the catalyst itself. In many instances for supported catalysts, nanoparticles sit within pores, making them difficult to detect and characterize by a number of techniques (TEM, SEM, XPS, XRD) [5]

In order to overcome these characterization barriers, model catalytic systems must be used that are optimized for proper characterization [24]. The most popular synthesis approach for model catalysts consists of techniques most commonly found in the semiconducting industry. These model catalysts are created using lithographic methods, chemical vapor deposition and or electron beam evaporation. These techniques are done by depositing nanoparticles atop flat supports such as silica (SiO_2) or amorphous alumina (Al_2O_3). In order for a model to be used it must withstand reaction conditions (stable nanoparticles) and have enough surface area for characterization and reactivity [24]. The model systems that were used for this study were prepared by spin coating and aerosol synthesis. This chapter describes the theory and background of spin coating and introduces aerosol synthesis.

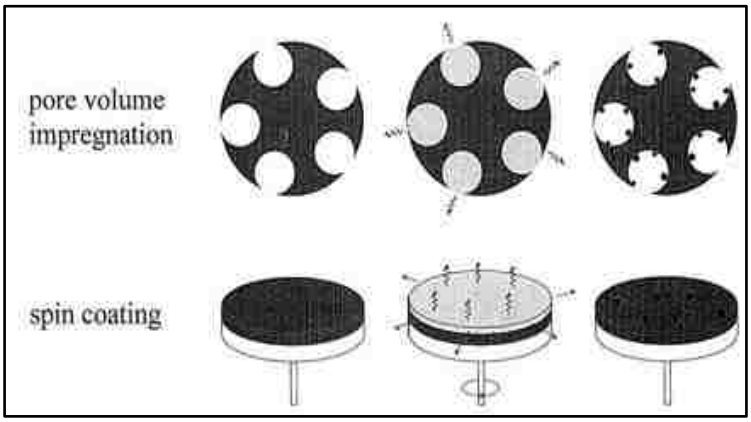

Figure 2.1. Similarities between pore volume impregnation and spin coating, capillary forces bring the solvent in the pores and the precursor evaporates. In spin coating the solvent forms a uniform layer, is deposited and the solution evaporates [5]

2.2 Spin Coating

Incipient wetness (pore volume impregnation) still remains the most commonly used industrial method to make catalysts. For this process, a solution of metal salts is deposited on a support according to its specific pore volume. Once the desired metal loading is reached, the catalyst undergoes a high temperature calcination treatment to remove the precursors. Since this method cannot be directly applied to flat supports for model systems, spin coating has been developed to mimic this process (Figure 2.1).

The spin coating process for the synthesis of nanoparticles was first developed by Kuipers [25] and Van Hardveld [26] and it has been well used throughout literature for the synthesis of model nanoparticle systems [3, 27]. Kuipers *et al.* [25] first demonstrated that it was possible to generate monometallic nanoparticles by "spin impregnation". This method calls for a metallic precursors dissolved in a volatile solvent such as n-butanol. The solution is deposited onto a flat surface and then spun to produce a homogenous distribution of nanoparticles.

2.2.1 Spin Coating: Fundamental Equations

These authors [3, 26, 27] demonstrated that this method yields nanoparticles on a flat surface with a narrow size distribution. Their work revealed that both the radial liquid flow and the evaporation of the solvent are the two main phenomena contributing to the formation of nanoparticles. The change in liquid film height (h) over time on the disk can be described by the equation of continuity for a pure fluid rotating under steady state conditions. Assuming a Newtonian fluid and an initial uniform thickness, Van Hardveled *et al.* [26] was able to derive the following equation:

$$\frac{dh}{dt} = -2\frac{\rho\omega^3}{3\eta}h^3 - \emptyset$$

Equation 2.1

With ω being the radial velocity of the spin coater, ρ and η being the density and viscosity and $\varnothing$ being the evaporation rate of the solvent. Where the evaporation rate ($\varnothing$) of the solvent from the rotating disk can be described by three transport phenomena:

1. Mass transfer of the fluid into the liquid/vapor interface.

2. The evaporation of the solvent at the interface

3.Mass transfer of the vapor phase

Due to constant airflow, the concentration of the solvent above the film will always be zero. The airflow above the film will remain laminar due to a relatively low Reynolds number.

The loading of the metal precursors (m) after spin coating can be then estimated by multiplying the critical height (h_1) by the initial solute concentration (C_o) [26]:

$$m = c_0 h_1 = c_0^3\sqrt{\frac{3n\emptyset}{2\rho\omega^2}}$$

Equation 2.2

2.2.2 The Effect of Humidity on Spin Coating

Their experiments also demonstrated that this method requires quick drying solvents while simultaneously minimizing the presence of water during the process (Figure 2.2). The wetability of the solvent on the wafer also has been found to have a significant impact on the uniformity of the nanoparticles. [3, 25-27] They found that poor wetability results in small droplet formation, causing a poor distribution of nanoparticles. The authors concluded that this is due to the high contact angle of the solvent on the flat surface [3, 25-27].

A number of other factors have been investigated to control size and loading of the nanoparticles on the flat surface, these techniques include changing radial velocity and functionalizing the surface of the wafer [3, 25-27]. Although these optimization parameters are beyond the scope of this study, it would be of great interest to apply these to future model bimetallic systems synthesized via spin coating.

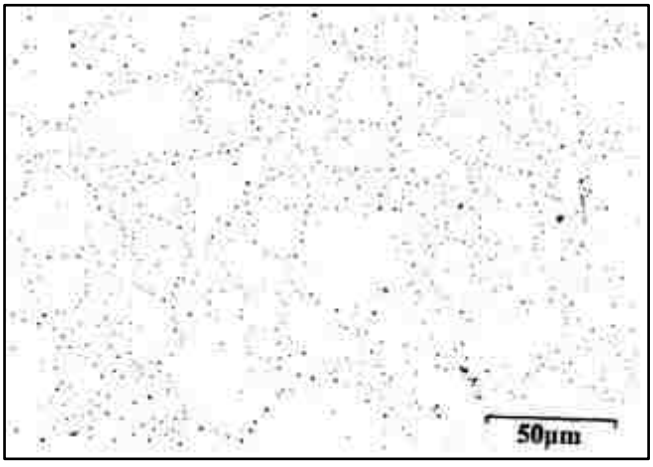

Figure 2.2. Uneven distribution of Cu nanoparticles from spin coating as result of aqueous solvent [3]

2.4 Aerosol Synthesis

Another method used specifically within our research group as a model system involves unsupported metal powders. Traditional methods to make supported metal catalysts usually contain less than 10 wt% of the active species supported on various oxide supports. This can make characterization of both the active phase and active phase transformation difficult. These oxide supports are electrically insulting leading to loss of signal for a number of characterization techniques including XRD and Raman Spectroscopy [24]. Model systems described previously are also great candidates to understand fundamentals but their relatively low surface area make reactivity studies difficult. Fortunately, using unsupported aerosol powders can overcome these obstacles.

Aerosol synthesis has been used specifically for the bimetallic PdZn system [18, 28]. This method allows one to prepare phase pure PdZn homogenous bimetallic powders with surface areas suitable for reactivity studies (1-10 m^2 per gram). These high surface areas and lack of support yields samples suited for phase transformation studies that can coincide with reactivity measurements [18]. The concentration of the powders can also be easily changed depending on the concentration of the initial precursors. Detailed mathematical models describing the mass transfer of aerosol synthesis which are beyond the scope of this work can be found in reference [29].

These two methods for the synthesis of model catalysts were instrumental in understanding the first steps of active phase transformation synthesis along with mapping out crucial transformations for the bimetallic PdZn systems. The conclusions obtained will be presented in later chapters.

Chapter 3.

Characterization Techniques

3.1 Characterization

Throughout this work a number of characterization techniques were used, this chapter is an introduction to the tools used in the order of most applied.

3.2 Electron Microscopy

3.2.1 Transmission Electron Microscopy

Transmission Electron microscopy (TEM) has headed the nanocharacterization revolution. Its advances over the past century have lead to fundamental understandings in a number of fields including semiconductors, catalysis and material science. Electron microscopes were first developed in order to surpass the resolution of traditional light microscopes, which are limited by the wavelength of visible light. The increased resolution, advances in equipment and sample preparation, have made TEM a viable tool for heterogeneous catalysis and the most valuable technique of characterization for the following studies in this dissertation [30, 31].

Overall resolution, which is defined as the smallest distance that can be resolved in a light microscope (VLM) is determined by the Rayleigh Criterion. This value (δ) is given by equation 3.1.

$$\delta = \frac{0.61\lambda}{\mu \sin \beta} \quad 3.1$$

Where λ is the wavelength radiation, μ is the refractive index of the viewing medium and β is the semi-angle collection of the magnifying lens. For green light the minimum resolution is around 300 nm, although small, much detail is lost in this regime. This limited resolution demonstrates the great need for TEMs for nanocharacterization. TEMs surpass VLMs due to the wavelength of an electron, which is much smaller than that of visible light, at 4 pm it is smaller than a diameter of an atom. In TEMs the best resolution can be described by equation 3.2.

$$\delta = \frac{1.22\lambda}{\beta} \quad 3.2$$

TEMs are not limited by the wavelength of an electron but rather by aberrations in the electronic lenses. Recent developments in aberration correction have pushed the resolution of TEMs below the 0.1nm barrier [30].

The High Resolution Transmission Electron Microscopy (HRTEM) conducted in these studies were performed on microscopes using field emission tungsten (W) guns as a source of electrons; field emission guns provide more monochromatic electrons when compared to thermionic sources. A typical operational energy range of a TEM is 200-300 keV operating under a vacuum of 10^{-6} mbar. [30].

Unlike VLMs the electronic lenses are fixed and must by adjusted by changing the strength of the lens. Most of the lenses used in TEM are electromagnetic therefore to change

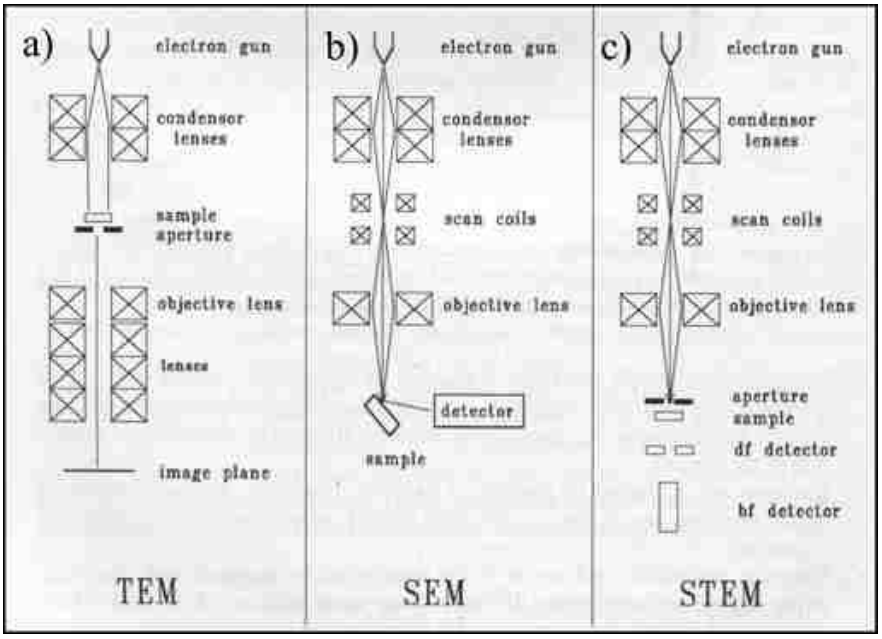

Figure 3.1: Electron Microscopes: a) TEM b) SEM c) STEM [28]

the strength the magnetic field must be altered. There are many lenses that can be adjusted in the microscope that are used to form an image. This is done by either magnification, demagnification or by forming a diffraction pattern (DP). An electron lens is composed of a cylindrical core made up of magnetically soft iron. This soft metal is called the pole piece. Coils of copper wire surround the entire cylinder. As the electrons enter the cylindrical piece through the bore their path is controlled by the magnetic field created in the lens. As the electrons enter the field they rotate around a vertical axis and spiral down the lens field. As electrons enter with higher keV, stronger lenses must be used to control their ray paths[30].

Figure 3.1 shows three types of electron microscopes. The TEM (Figure 3.1.a) is portrayed with an electron gun, various lenses, aperture and image plane. As the high intensity beam leaves the electron gun it passes through the lenses described above and an objective aperture, which is larger than the electron beam itself. The objective aperture allows one to control the resolution, depth of focus, and contrast of the imaged formed. After passing through the sample and various lenses below, a 2-D projection of the sample is formed on the phosphorus screen. The magnified image is called a bright field (BF) image

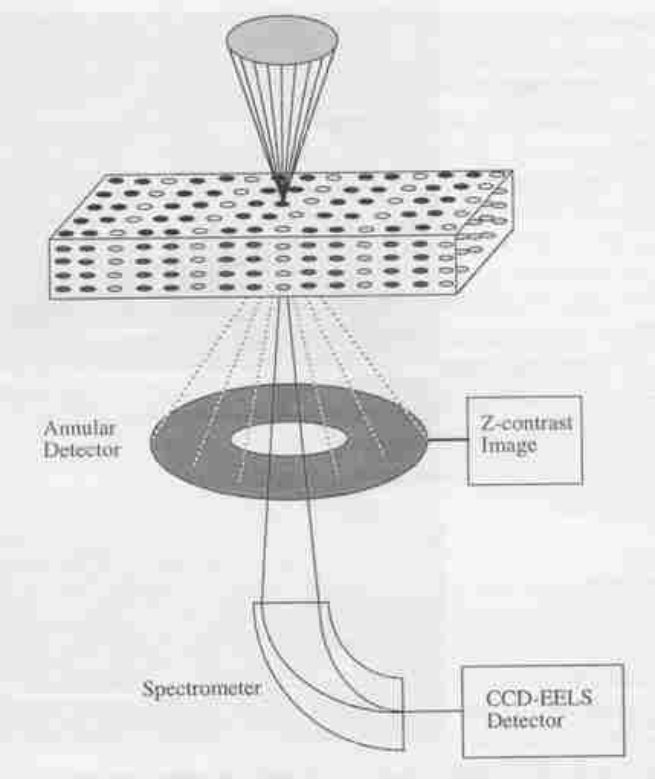

Figure 3.2 Annular STEM Detector [27]

[32]. In BF imaging all the diffracted electrons are excluded from imaging, this mode is preferred for detecting metal nanoparticles at low magnification, dark field (DF) imaging however, uses only the diffracted electrons. In order to obtain the DF image, the centralized beam must be blocked by an objective aperture [31].

3.2.2 Scanning Transmission Electron Microscopy (STEM)

In 1966, A.V. Crew was the first to propose the idea of a field emission electron probe tip [33]. His idea was that using a field emission source rather than a thermionic source would allow researchers to overcome the existing limitations on resolution in STEMs. Two years later he went on to design this field emission electron probe [34]. His new design further decreased the size of the probe from 70 Å to 50 Å.

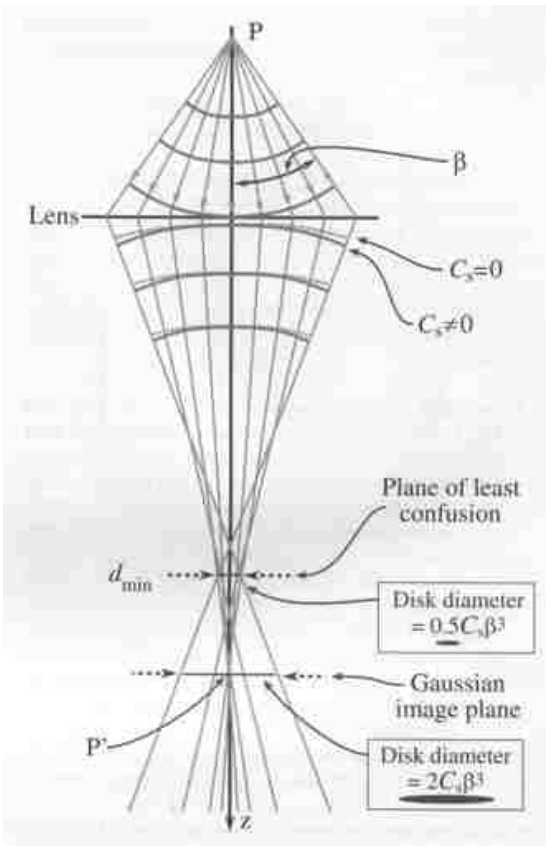

Figure 3.3 Formation of annular region caused by C_s in TEM [31]

In STEM (Figure 3.1.c) the diffracted beam is focused within an angular range, and an annular detector is used to form the ADF image (Figure 3.2). The annular detector consists of an annular sensitive region, which detects the electrons. The detector can have an inner radius of a few tens of milliradians, where the outer could have up to 100 mrad [35] . Today with aberration correction, probes can be less than a nm or smaller. STEM imaging is based off of Z (Atomic Number) contrast, meaning that the intensity of the electrons scattered at high angles follows a Z^2 dependence corresponding to the Rutherfrod scattering cross-section. The images are usually referred to as Z-contrast images with heaver elements appearing brighter, making this technique suitable for studying supported nanoparticles [31].

A majority of TEMs have a STEM mode available where the annular detector can be removed according to the mode desired. In the STEM configuration the detector forms the image while the transmitted beam can be used for elemental analysis [31].

3.2.3 Aberration Correction

Aberration is a common problem for a number of microscopes. In TEMs the aberrations present have a major effect on the overall quality of the image. Fortunately, these aberrations can now be corrected, resulting in much clear images. Figure 3.3 demonstrates the affect of spherical aberration. Spherical aberration takes the electron beam off axis resulting in a blurred image. In fact, due to the aberration, the image is actually a central high intensity region surround by a halo of decreasing intensity. Spherical aberration must be accounted for in the objective lens since the decreased quality is intensified by the other later lenses [30].

Correcting for this abberation in the TEM has led to the development of C_s correctors. A C_s corrector works by lowering the C_s coefficient for a lens, which is usually less than a few mm. The C_s coefficient is a term in the equation that describes the radius of the spherically aberrated disk (r_{sph}) (Equation 3.3).

$$r_{sph} = C_s \beta^3 \quad (2.3)$$

Where β can be described as the objective lens' angle of collection. For typical TEMs the C_s value is between 1-3 mm, however when a corrector is used, the C_s value decrease to less then 1 mm. This is done by redirecting the off axis beam such that it re-converges to a point rather than a disk. These recent advances in aberration correction have allowed the

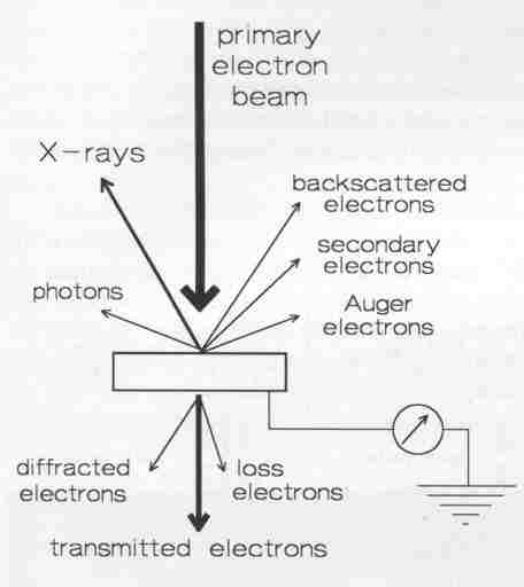

Figure 3.4 Characteristic signals emitted by a sample when exposed to an electron beam

development of HRTEM/STEM that currently push the 0.1 nm barrier allowing for detailed atomic resolution images[30].

3.2.4 Elemental Analysis via Electron Microscopy

Figure 3.4. demonstrates the number of detectable singles that are emitted from a sample when it encounters an electron beam. Although many, the primary signals that were used for elemental analysis in the TEM for these studies involve characteristic x-rays [31].

3.2.4.1 Energy Dispersive X-Ray Analysis

All elements experience x-ray florescence. X-ray florescence occurs when a core shell electron is lost and an electron of higher energy falls to fill its place. The released characteristic x-ray photon has a specific kinetic energy. For EDX this characteristic photon is detected by an EDX detector. The sampling area depends on the electron beam size. For scanning electron microscopy (SEM), which will be described later, the sampling area is

Figure 3.5 Image of JEOL 2010F STEM at the University of New Mexico

between 5-10 nm. For an aberration corrected STEM the sampling area depends on the probe size, which can be easily less than 0.1 nm. [32].

3.2.5 TEM/STEM/EDX Equipment

HRTEM, STEM, and EDX for these works were performed on a JEOL 2010F (Figure 3.5) at the University of New Mexico operating at 200 kV with an electron probe size of 1 nm. Aberration corrected HRTEM and STEM were performed at Nelson Mandela University in South Africa on a JEOL ARM 200F (Figure 3.6) operating at 200 kV with a probe size of 0.08 nm giving detailed atomic resolution images

Figure 3.6 Image of aberration corrected JEM ARM 200F (ASU)

Extensive EDX maps were performed on a FEI Tecnai Osiris (Figure 3.7) equipped with 4 EDX detectors operating at 200 kV. The multiple detectors allow for detailed elemental mapping that can acquire high quality spectra in seconds rather than minutes when compared to the JEOL 2010F.

3.2.6 Scanning Electron Microscopy (SEM)

Scanning electron microscopy is another valuable technique used for the study of heterogeneous catalysis. SEM utilizes a focused probe, that moves in a raster pattern across a

Figure 3.7 Image of FEI Tecnai Osiris

sample. The images are obtained from the backscattered and secondary electrons detected by a cathode ray tube that is in sync with the raster probe. SEMs are generally lower in energy (<100Kev) compared to TEMs and provide detailed surface information. One drawback of SEM is that it is limited by the size of the incident electron beam [31].

3.3 X Ray Diffraction (XRD)

XRD provides information over phase, composition and average crystallite size for a powdered sample. An XRD pattern is obtained from the elastic scattering of X-Ray photons in a periodic lattice [32]. The lattice spacing (*d*) of a particular lattice can be obtained by

measuring the angle of the constructive interference that leaves the crystal according to the Bragg relation (Equation 2.5)

$$n\lambda = 2d \sin\theta \quad (2.5)$$

Where λ is the wavelength of the x-rays, θ is the angle between the incoming X-rays normal to the reflecting lattice plane and n is an integer called the order of reflection. A stationary x-ray source (Cu Kα) is used to obtain the pattern. A movable detector measures the intensity of the diffracted radiation as a function of 2θ. Diffraction patterns of perfect crystals are narrow corresponding to large particles, smaller particles however are reflected in broad peaks. The overall crystallite size (L) relation to peak width and crystallite size is given by the Scherrer formula (Equation 2.6).

$$< L > = \frac{k\lambda}{\beta \cos\theta} \quad (2.6)$$

Where β is the peak width and k is a constant taken as 1 [32]. Even though XRD provides valuable information of phase and crystallite size, information can be lost due to peak overlap along with broad peaks corresponding to smaller particles. XRD itself is a bulk technique where nanoscale details can be lost [32].

3.4 X-Ray Photoelectron Spectroscopy (XPS)

XPS provides depth specific oxidation state information of the sample along with sample concentration. XPS is based from the photoelectric effect, photons from an x-ray source impinge on the sample causing photoionization to occur [36]. The XPS chamber must be maintained at pressures less than 10^{-6} torr to limit intensity loss in both the detector and

analyzer. Depending on the intensity of the incoming photon an electron can be ejected from the valance band or from both the valance band and core levels. From basic energy conservation one can determine the binding energy ($E^{'b}$) of the electronic level of the ejected photon (Equation 2.3). Where $E^{'k}$ is the kinetic energy of the photoelectron and hv is the incident photon energy.

$$E^{'k} = hv - E^{'b} \text{ (Equation 3.3)}$$

XPS spectra are plotted as a function of binding energies. The peaks obtained are usually matched with the help of an energy table, where the location of the peaks correspond to the quantum numbers of the levels from which the electrons were ejected [32]. Oxidation states are determined by binding energy shifts of the peaks obtained. Sampling depths of XPS varies (1.5 – 6 nm) depending on the kinetic energy of the photoelectron [32]. Care must be taken when performing peak integration to account for any lost intensities due to the nature of the samples themselves. At times decomposition of overlapping peaks must be performed by least square fitting parameters, which can sometimes be caused by multiple phases on the surface of the sample. Also, when performing XPS, charging of the sample must be accounted for due to the effect it has on peak shift for the spectra.

3.5 Raman Spectroscopy

Raman Spectroscopy is based of the inelastic scattering of photons from mono chromatic light (lasers 500-600 nm). Inelastic scattering occurs when photons are adsorbed and energy is lost by excitation and vibration of the adsorbed structure. The measurements of these changes of energy states of the photons either being zero (Rayleigh), negative (Stokes), and positive (ant-stokes) give characteristic bands [32]. These different changes give

information corresponding to the vibrational modes of the system being measured. These different vibrational modes are unique to different chemical compounds. The scattering also gives information corresponding to the crystal structure. The use of a focused laser can reduce the spatial resolution to around 1 μm [36].

Unfortunately Raman is limited by the small cross section of Raman scattering, where a number of peaks are lost due to the Rayleigh band, however using a higher intensity laser can increase the size of the peaks. Still for a number of samples fluoresce is an issue leading to a large spectral background [32].

Chapter 4

Experimental Methods

4.1 Model Catalyst Synthesis

4.1.1 Spin Coating

The flat silica supports were made from Si(100) wafers that were diced into 1”·1” squares and then calcined at 750 °C for 12 hours at 15°C/min. The wafers were then cleaned using a H_2O_2/NH_4OH at 60°C etch and then hydroxylated in a boiling water bath for 20-30 minutes following the procedure described by Borgna [37]. Spin coating was done on a TC100 AG Desktop Spin Coater (Figure 4.1). Two equimolar PdZn solutions with different solvents and metallic precursors were synthesized in house for spin coating.

The nitric acid PdZn solution was synthesized by combining Pd and Zn nitrates, (Sigma Aldrich - 99.98, 99.99%) (12.5 mmol/L, 12.5 mmol/L) with 10 wt% Nitric Acid. Similarly, the PdZn acetate solution was synthesized by combining Pd, Zn and ammonium acetates (Aldrich - 99.98, 99.99, 97%) (12.5mmol/L, 12.5mmol/L, 50mmol) to glacial acetic acid (Aldrich, 99.7%). The addition of ammonium acetate was necessary in order to increase the solubility of Zn acetate in the glacial acetic acid [38]. Both the acetic acid and nitric acid solutions were spin-coated onto the SiO_2 supports in an inert dry nitrogen atmosphere at 3,000 rpm to lower the relative humidity. 75 micro liters of each solvent were deposited first to remove any dust on the surface followed by 75 micro liters of each Pd-Zn solution described earlier. The samples were then subjected to various heat and reduction treatments described in later chapters.

Figure 4.1 TC100 AG Desktop Spin Coater used for spin coating samples

4.1.2 Aerosol Synthesis

PdZn nanopowders were synthesized from PdZn precursors dissolved in 10-wt% nitric acid. The 10-wt% Pd nitrate nitric acid precursor containing 4.5-wt% Pd was obtained form Sigma Aldrich. The ZnO precursor (Sigma Aldrich) was dissolved in the Pd nitric acid solution. (The concentration of the final product is dependent on the PdZn mixing ratio). A schematic diagram of the aerosol synthesis is given in Figure 4.2. The nitrate precursors were atomized via a Walgreen ultrasonic humidifier by immersing a Nalgene bottle into the water reservoir. The droplets produced were carried through a 2.54 cm O.D. 80 cm quartz tube by an industrial air carrier gas at 1 liter per minute. The quartz tube was positioned inside a three-stage tube 80 cm tube furnace (600ºC, 700ºC, 600ºC) [28]. The droplets within the furnace went through various drying steps until the final product deposited on a Teflon filter. The aerosol system was ran until approximately 90% of the solution was expended. The

powder that had been deposited was removed from the filter and under went a heat treatment in 100 sccm of flowing air at 200°C for 2 hours to remove any residual nitrates.

4.2 Supported Catalyst Synthesis

AP 1wt% Pd/ZnO

The 1 wt% Pd/ZnO catalyst used for MSR reactivity and CO oxidation was

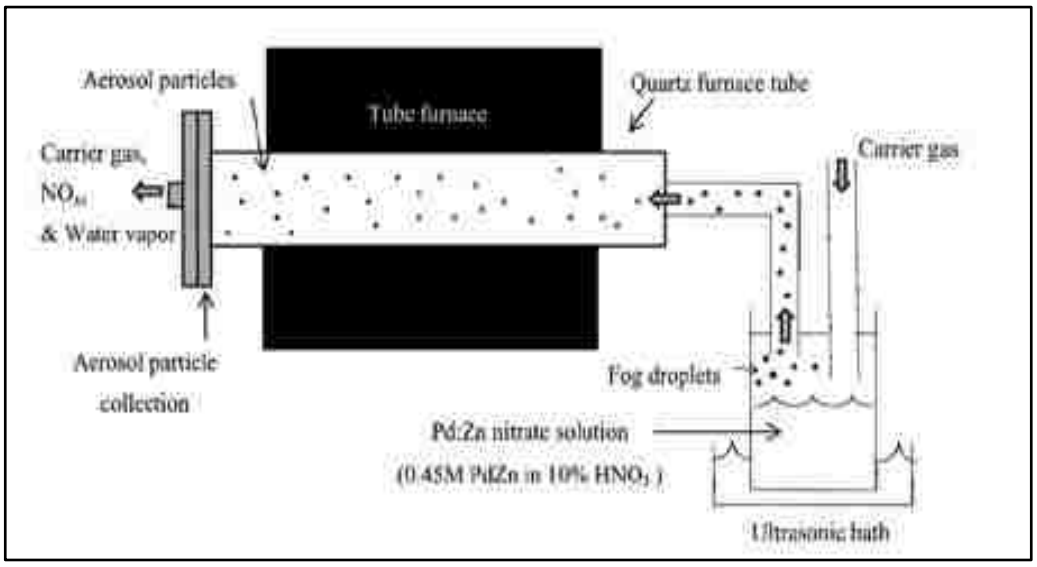

Figure 4.2 Schematic of Aerosol Synthesis setup

synthesized by the alcohol reduction method based off the approach described by Burton *et al.* [39]. Anhydrous $Pd(OAc)_2$ was dissolved in anhydrous methanol (3mM Pd Acetate). The solution was capped and left to dissolve in an ultrasonic bath. ZnO was added to the solution in a round bottom flask to achieve 1 wt% loading of Pd. The round bottom flask was then attached to a rotary evaporator where the sample was maintained until evaporation of the solvent and then dried over night at room temperature.

4.3 MSR and CO Oxidation reactivity measurements

Reactivity was performed in an in house built tubular packed bed reactor that could alternate between CO oxidation and MSR (Figure 4.3). The catalysts were crushed and sieved to 100 – 250 μm and then packed into a 4.95 mm i.d. 516 stainless steal tube, which served as the reactor. The reactor was inserted inside a programmable tube furnace. The temperature of the bed was measured by placing a K-type thermocouple on the catalyst bed.

The effluent of the reactor was analyzed using a Varian CP 3800 gas chromatograph (GC) equipped with a Porapak Q and a molecular mole sieve column. The GC operated in Series/Bypass mode for CO oxidation with He as a carrier gas. The analysis of the gas phase species of both CO and CO_2 were used to calculate conversion with GC sampling every 7 minutes. For MSR the analysis of the gas phase species CO_2, CO, CH_3OH, H_2 and H_2O along with a carbon balance allowed the methanol conversion and CO_2 selectivity to be calculated. The GC operated in Bypass mode with He as a carrier gas. The GC was programmed to sample the reactor product every 23 minutes.

The catalysts were reduced *in-situ* under various conditions and reacted as described in later chapters. For MSR reactivity measurements, the liquid reactants were fed at a 2:1 volumetric rate with He as an inert feed gas (75 sccm). The reactants were introduced by a high-pressure pump-vaporizer system (130°C) using MKS mass flow controllers. For CO oxidation 1.5 sccm CO, 0.8 sccm O_2 and 70 sccm as an inert feed (He) gas were fed into the catalyst bed.

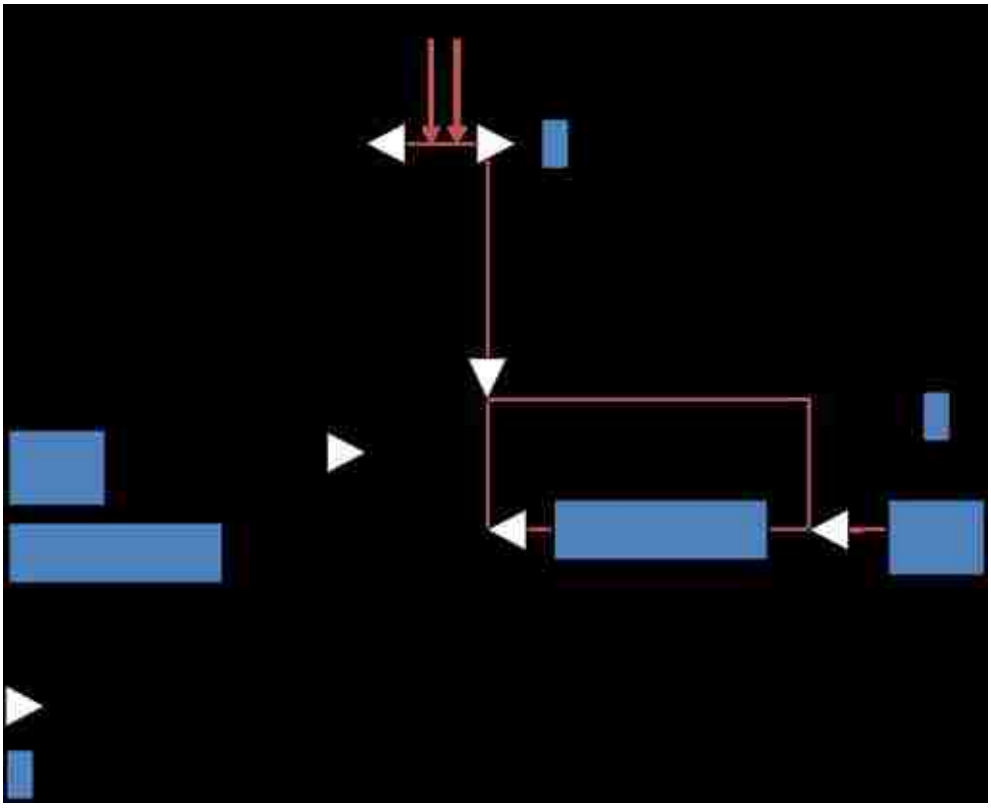

Figure 4.3 Flow Chart for MSR/ CO Oxidation System

Chapter 5.

Synthesis and Characterization of Oxide Precursors: (Pd,Zn)O and (Zn,Pd)O

5.1 Introduction

The binary PdZn system has been widely characterized. Its phase diagram is well defined with existences of the α and β intermetallic phases, along with solid solutions containing both excess Zn and Pd [28, 40]. Although the alloy itself is well defined, little is known about the mixed oxide precursors of PdZn, which are present when used as a catalytic system. Traditional methods to make PdZn catalysts usually contain less than 10 wt% of the active species. This relatively low weight loading makes characterization of the oxide precursors difficult.

In order to investigate the proposed hypothesis, we used aerosol routes to synthesize unsupported oxides to investigate the uniformity of the phase. Since treatment of these aerosol powders in a high temperature reducing41 environment (500ºC) yielded phase pure material, it was of great interest to synthesize the oxides via this route to see if the same is true for the powder in the oxide form [18, 28].

5.2 Experimental

5.2.1 Powder Synthesis

The Pd Zn mixed oxide powders were synthesized using an aerosol method described in reference [28]. Four precursor solutions were made by mixing various atomic Pd:Zn ratios of 100:0, 73:27, 59:41 and 39:61 respectively by combining 10 wt% Pd Nitrate Solution

(Sigma Aldrich) containing 4.5 wt% Pd in 10 wt% Nitric Acid with ZnO powder (Sigma Aldrich). The as prepared powders were collected from the aerosol setup and then calcined in 100 sccm of flowing air at 200°C for 2 hours to remove any residual nitrates.

4.2.1 Mixed oxide characterization:

TEM/SEM: Images showing surface morphology were obtained by SEM using a Hitachi S-5200 SEM. Low magnification TEM, HRTEM and EDX at various scales were performed on a JEOL 2010 FASTEM field emission gun microscope operating at 200 kV.

XRD: XRD patterns were acquired using a Scintag PAD V diffractometer operated at an accelerating voltage of 40 kV. Cu Kα x-rays were used for all structural studies in this experiment, and the wavelength used for all relevant refinements and calculations was 1.5040562 Å. A graphite monochromater was used to remove Cu K-β radiation.

Raman: Raman spectroscopy was conducted on an inVia Raman Leica microscope using a x20 objective. The samples were placed on a microscope slide, and the spectras were obtained using two lasers, a 514.5 nm Ar ion laser along with a 785 nm solid-state diode laser. Data was collected from 100-2000 cm^{-1} for 60 seconds. Each sample scan was conducted 5 times using a defocused beam of 50% with a laser power of 10% for the 514 nm line(16 mW) and 1% for the 785 nm line (100 mW). The final spectra for analysis were obtained by taking the average of 3 separate spectra. Wire Version 3.2 was used for instrument control and for data capturing. Pure Si was measured and used as a standard for calibration.

5.3 Results/Discussion

Overall atomic Pd:Zn concentrations acquired via TEM EDX are listed in Table 5.1. The amount of atomic Zn increases with each sample down the table with agreement of the prepared Pd:Zn nitric acid stock solutions.

Sample Name	TEM EDX Atomic Concentration %Pd : %Zn
PdO	100 : 0
3:1	73.2 : 26.8
1.5:1	59.3 : 40.7
1:1.5	39.3 : 60.7
ZnO	0 : 100

Table 5.1 Atomic concentrations of various mixed oxide samples obtained via TEM EDX

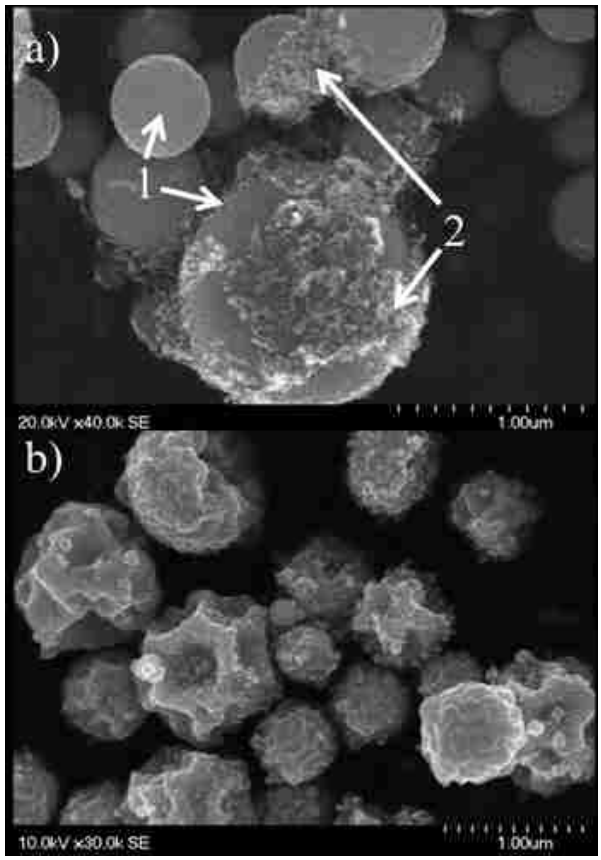

Figure 5.1. Morphology of powders after calcination at 200°C for 2 hours (Air 100 sccm) a) 3:1 b) 1.5:1 Pd:Zn

SEM Imaging of the powders with different Pd:Zn ratio reveals a drastic change in morphology as the Zn concentration is increased. Figure5.1 a. is an image of the 3:1 PdZn sample, the sample is composed of a dense spherical phase (Arrow 1) along with a second agglomerated phase on the surface of the spherical phase (Arrow 2). Due to the excess Pd, the bulk spherical phase can be attributed to bulk PdO and the agglomerated phase can be due to ZnO. As the ratio of Zn increase, 1.5:1 (Pd:Zn) the surface morphology of the bulk spherical phases changes drastically (Figure4.1 b.) Upon initial observation the amount of material of lighter contrast can be attributed to the increase Zn concentration.

SEM EDX of the regions described above show the differences of Pd:Zn concentrations (Figures 5.2 a & 5.3 b) in agreement with the stock concentrations and Pd:Zn ratios found from overall TEM EDX. However, variations across the sample can be seen with changes in morphology. For both the 3:1 and 1.5:1 samples (Figures 5.2 b, c & 5.3 b, c). The spherical aerosol powders that have a more uniform surface and are Pd heavy (Figures 5.2 b & 4.3 b) (~75 atomic %) whereas the spherical aerosol powders with rougher surfaces have slightly more Zn present (Figures 5.2 c & 5.3 c). From this EDX we can deduce that there is an existence of two separate oxide phases, one that is Pd heavy and one that contains primarily Zn.

Low magnification TEM (Figure5.4) reveals an increase in ZnO crystallites on the surface of the Pd rich phase due to the change in morphology as the Zn concentration is increased. This is the same change in morphology seen via SEM with increasing atomic Zn concentration. Small scale EDX was performed to confirm the existence of the two separate

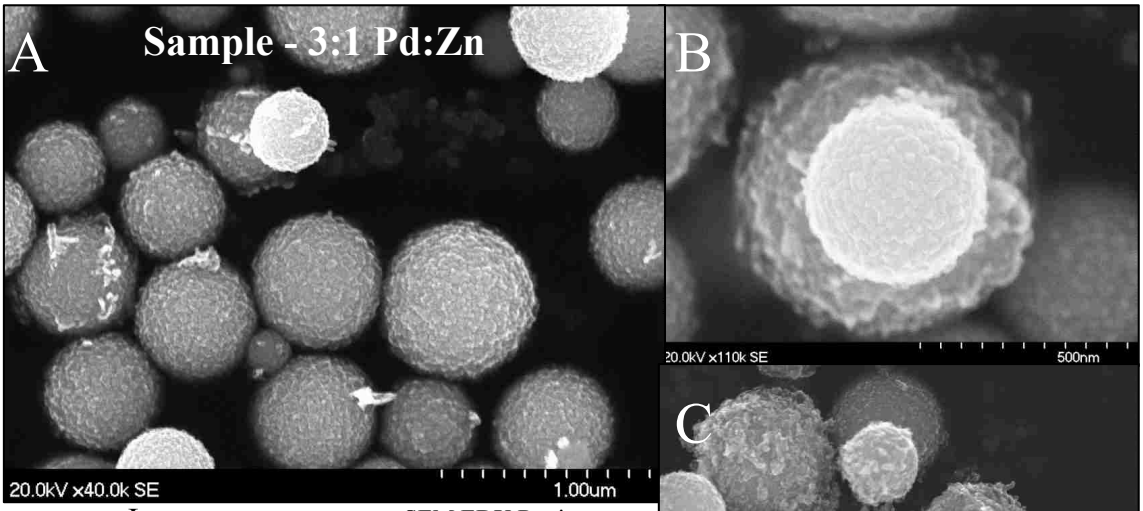

Image	SEM EDX Region Concentration %Pd : %Zn
Sample Area A	76:24
Sample Area B	78:22
Sample Area C	70:30

Figure 5.2 SEM EDX Region Concentration of 3:1 PdZn Sample

phases (Pd rich and Zn rich) seen via SEM. In order to isolate the various regions an objective aperture was used to decrease the sampling area of the beam in the TEM during EDX acquisition.

The atomic concentrations corresponding to the indicated (A,B,C,D) area can be seen in Table 4.2. Scaled EDX of region A of the 2:1 Pd:Zn sample shows the spherical Pd rich phase having a concentration of 76:24 atomic % Pd:Zn, region B also shows the same concentration. Scaled EDX of region D of the 1:1.5 Pd:Zn sample shows an increase of Zn concentration on the Pd rich spherical particles, corresponding to the change in surface morphology. Region D of the same sample shows a drastic increase in Zn concentration (88:12 atomic % Pd:Zn). The increase in Zn can be attributed the Zn rich oxide phases, the occurrence of Pd in the same area can suggest the isomorphic incorporation of Pd into the

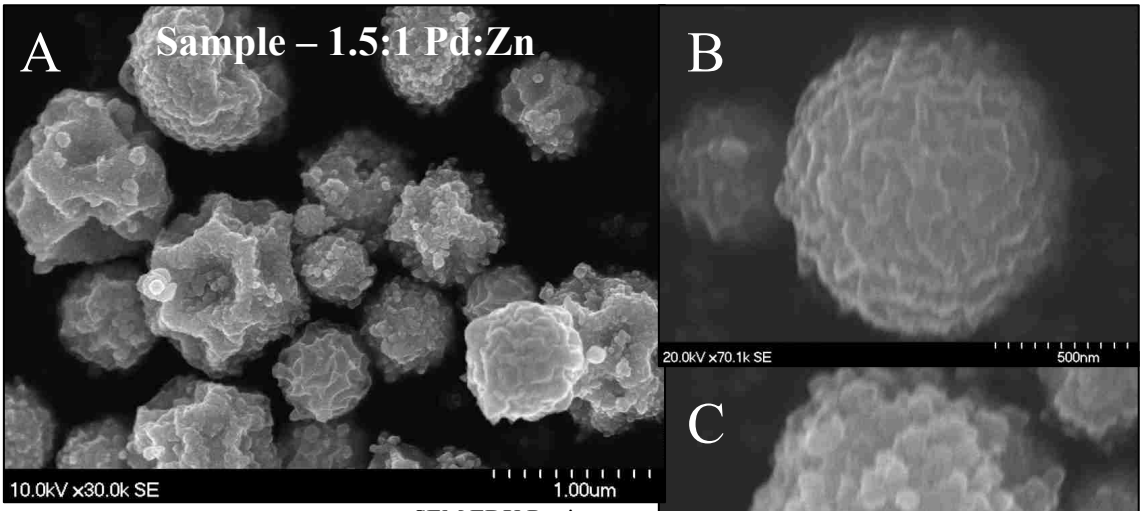

Image	SEM EDX Region Concentration %Pd : %Zn
Sample Area A	59:41
Sample Area B	75:25
Sample Area C	61:39

Figure 5.3 SEM EDX Region Concentration of 1.5:1 PdZn Sample

ZnO lattice, showing the first evidence of the occurrence of a (Zn,Pd)O mixed oxide phase or merely PdO deposited on the surface .

Reitveld refinement of the characteristic XRD peaks corresponding to PdO for the pure Pd sample revealed a PdO crystallite size of 20 nm. Refinement of the same peaks for the 59:41 Pd:Zn sample gives a PdO crystallite size of 5 nm. XRD refinement of the bulk composition yielded the heavy Pd phase to contain 75 at% Pd and 25 at% Zn TEM was used to confirm the crystallite size of this sample (Figure 5.5) found by XRD. The overlay of the peaks for each sample can be seen in Figure 5.6. The peak corresponding to the (101) plane at 34.36 2θ is extremely sharp for the pure PdO sample corresponding to the large crystallite size, peak broadening occurs once Zn is incorporated into the sample. This broadening is an indication of Zn incorporation into the PdO lattice leading to a smaller crystallite size. The

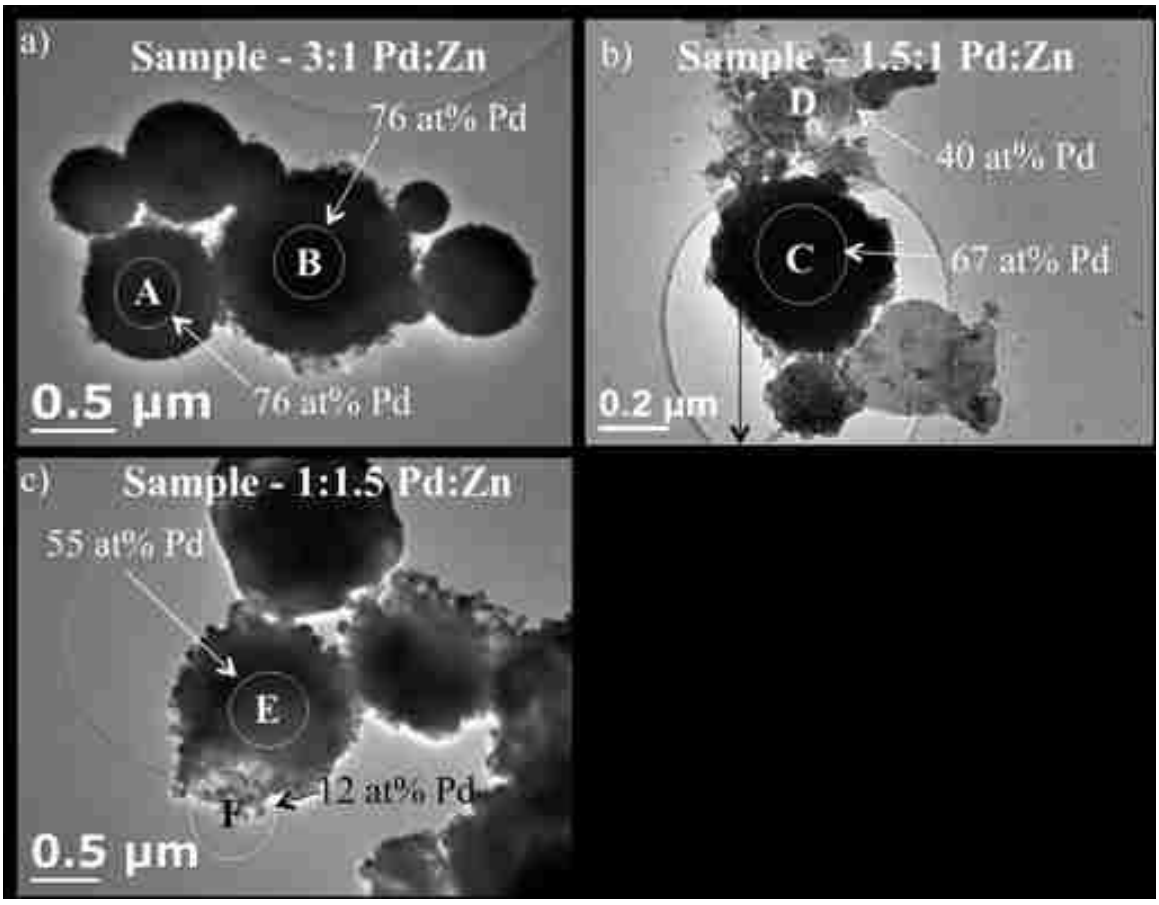

peak width remains relatively unchanged for each mixed oxide sample signifying a uniform PdO phase with Zn incorporation. The characteristic ZnO peaks at 31.76 (100), 36.26 (101) and 47.54 (102) 2θ grow with intensity as more Zn is incorporated into the sample, this is confirmed by the amount of amorphous material seen via TEM and SEM.

Figure 5.7 shows the Raman spectra obtained for each sample using the 514 nm and 785 nm laser lines. The resonance enhancement of the fundamental as well as combination and overtone bands of PdO when using the 514 nm laser can be seen. The bands at 441 and 643 cm^{-1} are the two fundamental PdO bands of E_g and B_{1g} symmetry respectively [41] All other bands present are non fundamental and are listed in Reference [41] In the 785 data of

PdO an extra band is observed at 275 cm^{-1} . It is assigned to be an overlap of the 1st overtones of a longitudinal acoustic (LA) and transversal acoustic (TA) mode [41]. For ZnO the fundamentals are observed at 99 (Not measured), 381,421 and 439 cm^{-1} and represent E_2^{low}, A_1, E_1, E_2^{high} modes respectively[41]. With all other non fundamental bands not referenced are listed in Reference [41].

All sets of spectra for the mixed oxides show the existence of the PdO main band at ~640cm^{-1} with a slight shift in the band for the samples that contain both Pd and Zn. The fundamental 441 cm^{-1} PdO band for the mixed oxide samples is slightly obscured by a newly observed broad feature at ~530 cm^{-1} for the 785 nm data, for the 514 nm data this broad band is shifted towards the maximum band position of ZnO with increasing Zn concentrations. The appearance of the broad band along with the shift allows us to deduce the solid solution substitution of Zn atoms into the D_{2h} site of the $P4_2/mmc$ crystal structure of PdO. For all

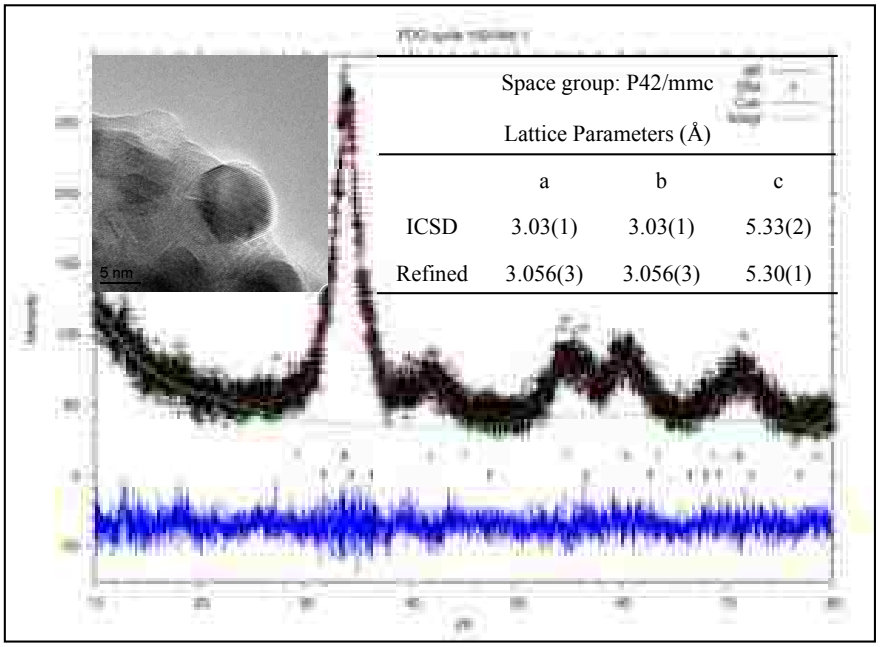

Figure 5.5 Reitveld refinement of the characteristic XRD peaks corresponding to PdO for the 59:41 Pd:Zn sample gives a PdO crystallite size of 5 nm. TEM was used to confirm the crystallite size of this sample

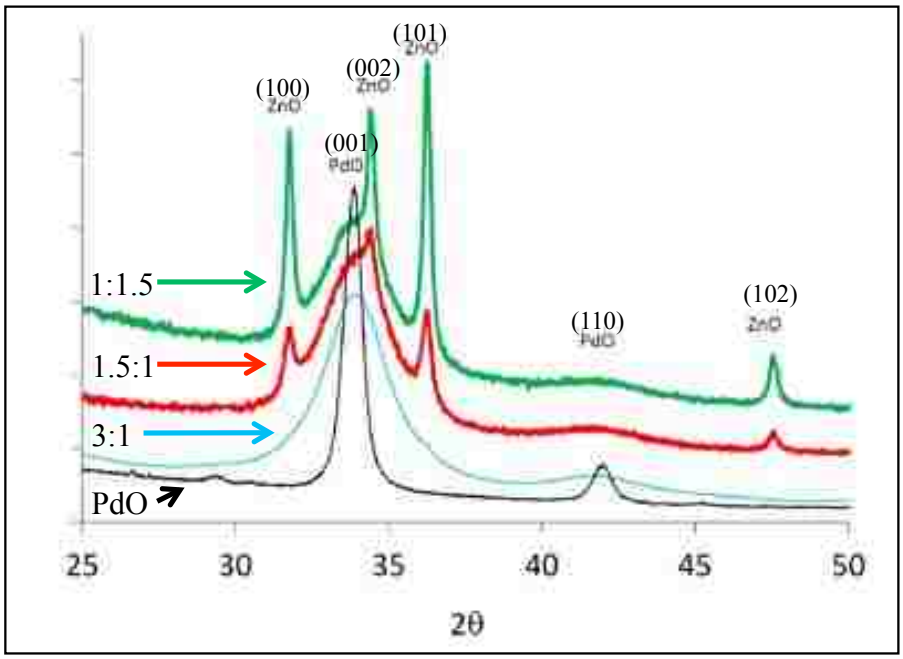

Figure 5.6 Overlaid XRD patterns for pure PdO and mixed oxide powders

mixed oxide samples the E_2^{high} mode for pure ZnO is not present. E_2^{high} modes are defect-induced modes associated with oxygen vacancies and or Zn interstitials. The loss of the E_2^{high} demonstrates a decrease in surface defects and oxygen vacancies due to Pd doping into the ZnO lattice [42]. The loss of the E_2^{high} peaks further demonstrates the existence of 2 phases, a (Zn,Pd)O with excess Zn and a (Pd,Zn)O with excess Pd.

5.4 Conclusion

Although aerosol synthesis yields a uniform phase pure material after high temperature reduction, here we have demonstrated through combined characterization techniques the existence of 2 mixed oxides, a previously undocumented (Pd,Zn)O and a greater characterized bulk (Zn,Pd)O. TEM and SEM were used to show two distinct phases of different morphologies and EDX showed the differences in Pd and Zn ratios for each phase of different morphologies. XRD was used to demonstrate the change in unit cell

volume of PdO and Raman was used to show incorporation of Pd into the ZnO lattice. This

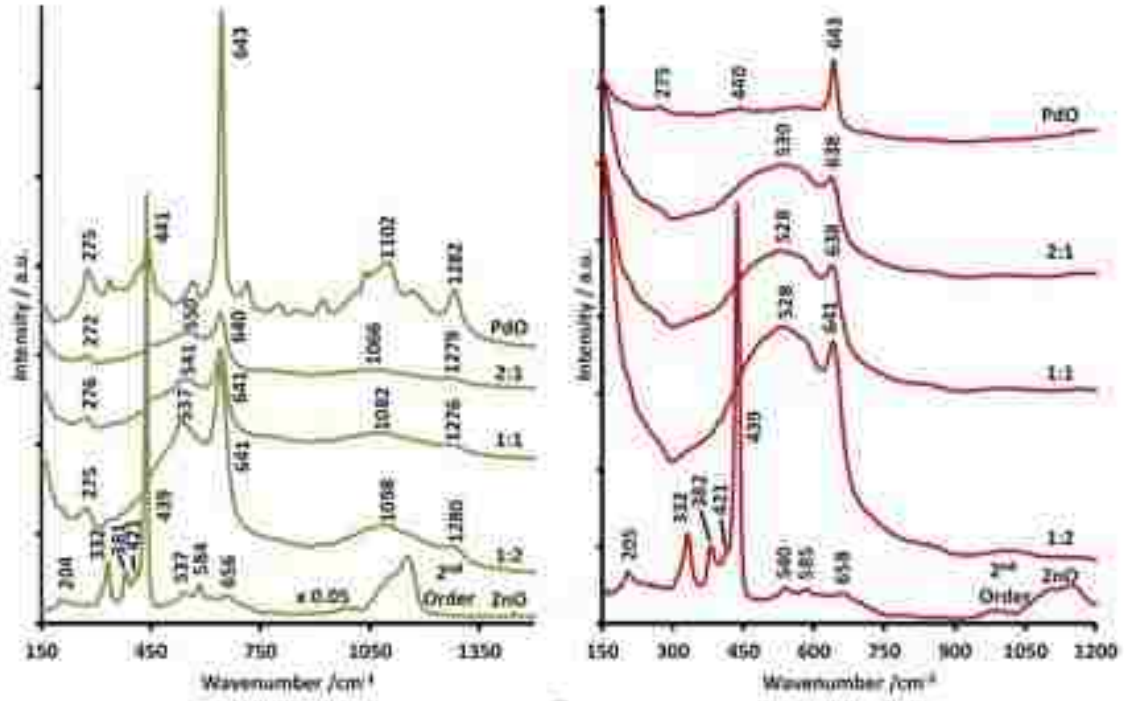

Figure 5.7 Overlaid Raman spectras obtained using a (a) 514 nm and using a (b) 785 nm laser line for each sample

study provides insight into the starting material of the highly active β1-PdZn that cannot be studied in supported PdZn catalysts.

Chapter 6.

Model catalysts for the study of phase evolution in bimetallic nanoparticles:

Transformation of a mixed Pd + Zn oxide to a thermodynamically stable Pd_2Zn

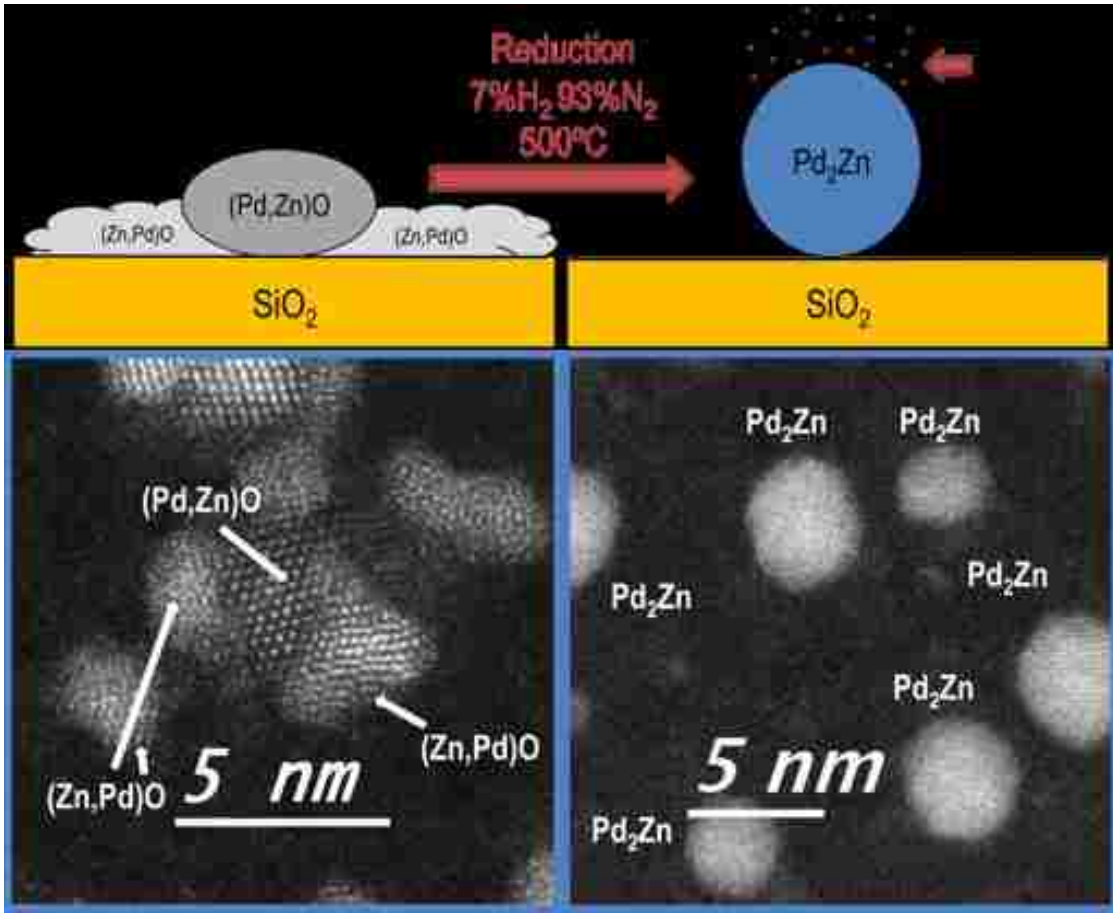

Figure 6.0 Overview of study. Nanoparticles were synthesized via spin coating and their phase was tracked from a mixed oxide to Pd_2Zn

6.1 Introduction

The phase and composition of a bimetallic catalyst plays a major role in determining activity and selectivity. Small sized particles on supported catalysts can be studied very well by x-ray absorption spectroscopy (XAS) but this technique averages information over the sample. The averaging of information makes it less suitable for phase evolution studies when multiple phases are present [43, 44]. A local technique such as TEM is ideal but generally provides poor statistics, since only metal particles in the thinnest regions of a typical supported catalyst can be studied [13, 19].

A model catalyst (flat, uniform thickness) allows for improved statistics since a large number of nanoparticles can be studied. Model catalysts based on thin oxide films have been used in previous work to gain insight into the evolution (catalyst sintering [45]) and also compositions of bimetallic nanoparticles [46]. However, a majority of these approaches deposit the metals via physical vapor deposition [46] not via liquid phase routes.

Thus there is a need for model catalysts synthesized using aqueous precursors that can provide insight into the formation and stability of metallic nanoparticles relevant to heterogeneous catalysts that can be used in the TEM [24].

Unfortunately, the small size of individual TEM grids (3 mm) makes them unsuitable for preparation via liquid phase routes. Also, TEM grids generally have steps and indents making them unsuitable for spin coating. We therefore in this study used a novel form of model catalysts developed by Thüne and coworkers that are fabricated using Si based micro-fabrication technologies [47] composed of a square sample containing 36 TEM grids (2 cm x 2 cm) with a flat surface, so it can be easily mounted

Figure 6.1. TEM grids fabricated using Si based micro-fabrication technologies composed of a square sample containing 36 TEM grids (2 cm x 2 cm). The flat surface of the wafer makes the samples suitable for spin coating. The 4" wafer is broken up to a 20 mm X 20 mm square where spin coating is preformed and further broken into the individual TEM grid.

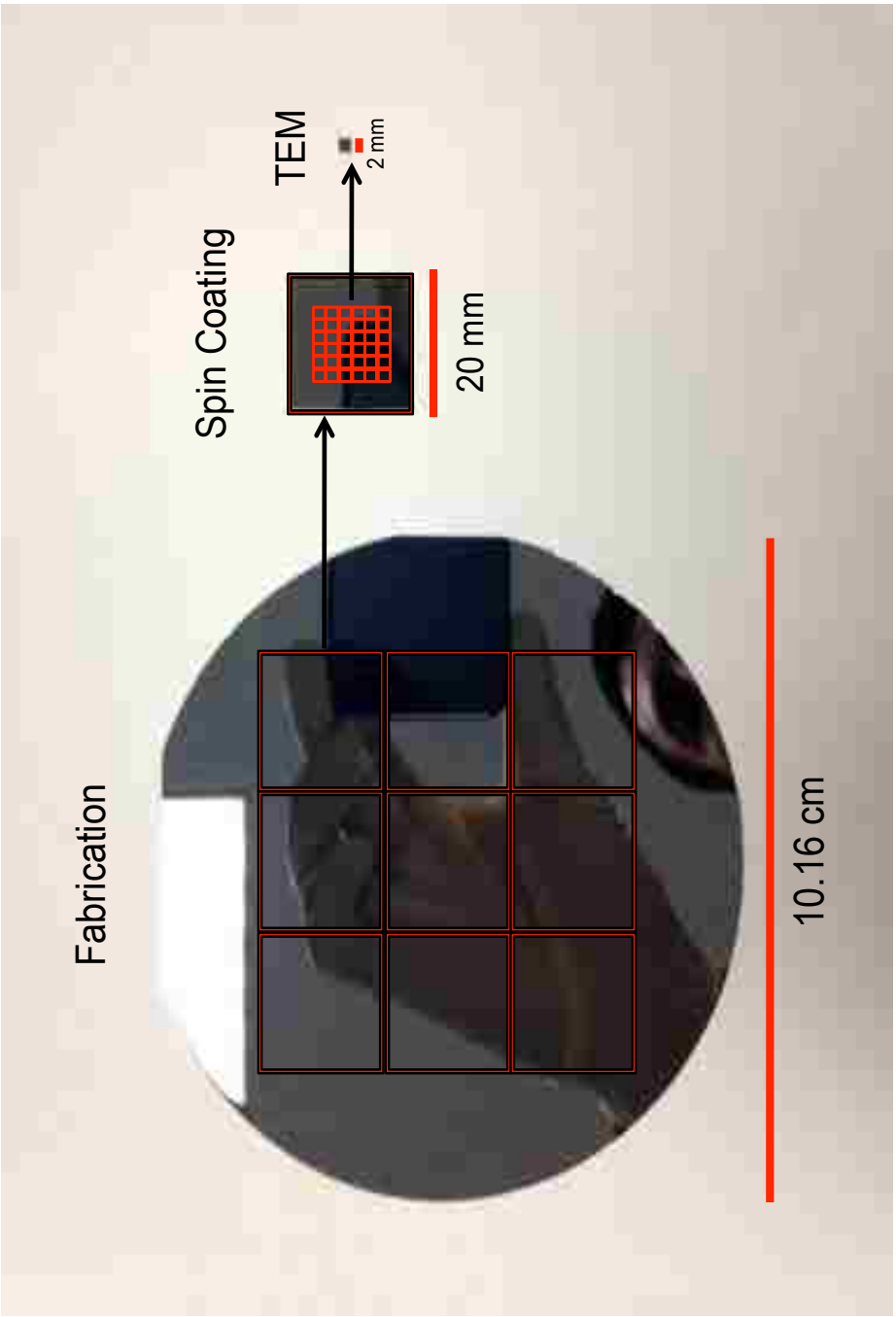

for spin coating. After the precursors have dried, the sample is broken up into 36 individual TEM grids that can then be subjected to all of the catalyst preparation steps, such as calcination and reduction, which are typically used in heterogeneous catalysis (Figure5.1). Being made of Si with a Si_3N_4 window and only a thin film of native oxide, the grids do not charge up when exposed to the electron beam, providing an ideal substrate for study by aberration corrected TEM and EDS mapping. Individual grids can also be studied using focusing XPS and by micro Raman making these grids an ideal platform for the study of phase evolution in complex heterogeneous catalysts.

Iwasa et al. [6] did seminal work on Pd/ZnO demonstrating the excellent CO_2 selectivity from MSR after high temperature reduction in flowing H_2. From Iwasa's work, it was thought to be necessary to heat the sample to 500 °C to form the intermetallic PdZn, but a number of recent studies have shown that high selectivity for MSR can be obtained even after lower temperature treatment [19].

Here we highlight the use of this model catalyst to map out the phases in the PdZn system as a function of treatment temperature and to understand the pivotal phase transformations that lead to increased activity and deactivation for MSR.

6.2 Experimental

6.2.1 Synthesis of Model Pd-Zn/SiO_2 Catalyst

We used custom made silicon wafers developed by Thüne and coworkers [47, 48] that were prepared via micro-fabrication to serve as model catalysts. The micro-fabrication involved the deposition of silicon nitride both at the back and front of a standard silicon (100) wafer. The nitride at the back was patterned to form an appropriate

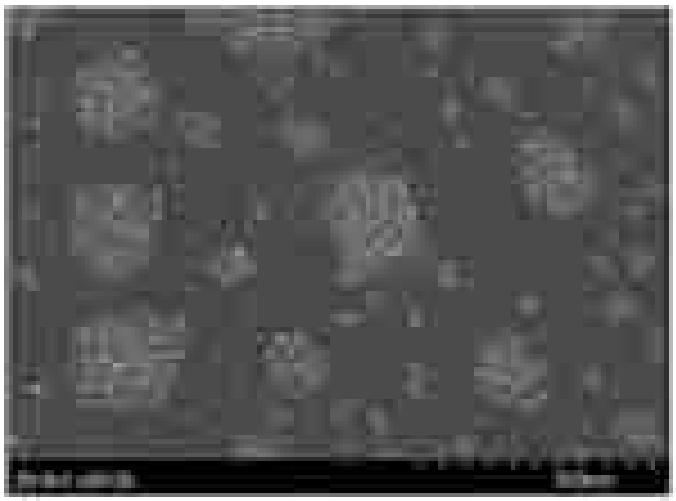

Figure 6.2 SEM image of Pd-Zn/SiO_2 sample with nitrate precursors/ 10wt% Nitric Acid Solvent
Calcined - 450˚C 100 sccm (air)
Reduced- 500˚C 100 sccm ($7\%H_2/93\%N_2$)

Figure 6.3 SEM image of Pd-Zn/SiO2 sample with acetate precursors, Glacial Acetic Acid Solvent
Calcined - 450˚C / 100 sccm (air),
Reduced- 500˚C / 100 sccm ($7\%H_2/93\%N_2$)

mask that facilitated anisotropic etching of the silicon until the silicon nitride at the top was left suspended in its framework. The silicon nitride layer on the top was made as thin as possible (~20 nm) to facilitate efficient TEM observation. A silica surface layer of about 3 nm thickness was formed by calcining the wafer in an oven at 750 °C for 24 h. The silica TEM grids used for our model catalysts were made to have a window with dimensions of 100 μm· 100 μm to allow for stability and adequate TEM imaging area. The silica TEM grids are robust and can survive high reaction temperatures and gas flows and are suitable for sample preparation via spin coating. Each silicon wafer was patterned so that 6 sets of 36 TEM grids were located on a sample of roughly 20 mm x 20 mm (Figure5.1).

Pd-Zn/SiO_2 bimetallic model catalysts were prepared through a wet chemical spin

coating approach using one of the 20 mm x 20 mm pieces from the microfabricated Si(100) wafers described above. This silicon wafer was then broken up into individual TEM grids, which were subjected to further treatments. This is the first report of aberration corrected TEM of model catalyst prepared via spin coating with the goal of achieving uniformity of composition and size to understand phase transformations. Solutions of Pd and Zn with acetates and nitrates as precursors were prepared to find the optimal solution for spin coating on the TEM grids. Both solutions were first spin-coated onto an 1" X 1" square Si(100) wafers described in the previous experimental section. The spin coating was performed in an inert nitrogen atmosphere at 3,000 rpm. 75 micro liters of acetic acid for the acetates and nitric acid for the nitrates were deposited first to remove any dust on the surface followed by 75 micro liters of the Pd-Zn each solution described previously. SEM showed that the sample using Pd, Zn nitrates (Aldrich, 99.99%) dissolved in nitric acid resulted in large agglomerated material lacking nanoscale uniformity after calcination at 450˚C and reduction at 500˚C (Figure5.2). Using acetates as precursors however resulted in a uniform distribution of nanoparticles (Figure6.3). The spin coating technique was then replicated using the model TEM grids with the Pd, Zn acetate precursors. After calcination at 450˚C for 1 hour under flowing air TEM revealed that the nominal size of the nanoparticles prepared via acetates was 3.9 nm. After reduction at 500˚C there was only a slight decrease in size demonstrating the stability of this model Pd-Zn system (Figure6.4).

6.2.2 Catalyst pretreatment

Following spin coating, the wafer was calcined in 100 sccm of flowing air at 450˚C for 1 hour. After calcination the wafer was broken into individual TEM grids and reduced in a quartz tube furnace under a flowing 100 sccm gas mixture for 15 minutes containing 7% H_2

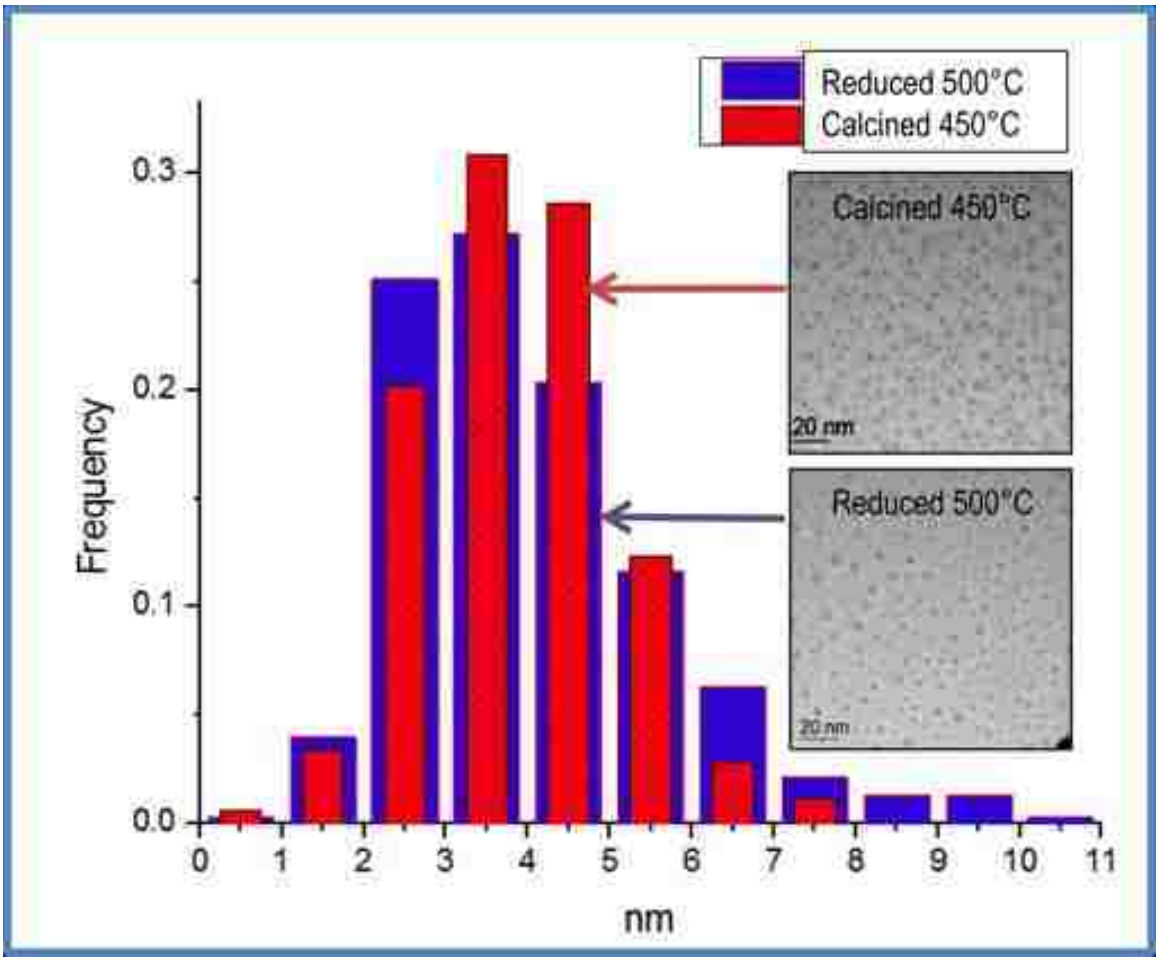

Figure 6.4 Particle size distribution for the Pd-Zn/SiO_2 model sample after calcination at 450°C for 1 hour (average size 3.9 nm) and after reduction at 500°C for 15 minutes under 100 sccm of 7% H_2/93% N_2 (average size 3.8 nm)

/ balance N_2. Each grid was reduced at its specified reduction temperature increasing with 100˚C increments to the final temperature of 500˚C for 15 minutes.

6.2.2 HRTEM/STEM & EDX Characterization

High-resolution scanning transmission electron microscopy (HRSTEM) was performed on each sample after calcination and reduction treatments on a JEM ARM 200F (JEOL) aberration corrected field emission transmission electron microscope operating at 200kV.

STEM images were recorded using a high angular dark field detector (HAADF). Lattice fringe analysis was used to determine the crystalline phases of the individual nanoparticles after reduction. Only particles that showed cross fringes were used to determine phase since Pd(111) and PdZn(111) lattice spacing are very similar, 2.246 and 2.19Å respectively, and hence cannot be distinguished if only one dimensional fringes are available. HRSTEM images were analyzed using Gatan Digital Micrograph with additional scripts (Diffractogram and Peak [49]) to make it possible to obtain contrast enhanced diffractograms and direct readout of lattice spacings from the peaks. The diffractograms were analyzed using Carine Crystallography 3.1 [50] to determine the angle between neighboring planes during cross fringe analysis of the individual nanoparticles. Particle size distributions were obtained from low magnification transmission electron microscopy (TEM) and STEM images acquired on a JEM 2010 FASTEM (JEOL) field emission gun scanning transmission microscope operating at 200kV.

High-resolution energy dispersive X-ray spectroscopy (EDX) mapping was performed on a FEI Tecnai Osiris equipped with 4 EDX detectors operating at 200 kV. Overall compositions were determined at various scales by EDX in TEM mode performed on a JEOL 2010 FASTEM.

6.2.3 Focused XPS and Micro Raman

XPS spectra were acquired on each TEM grid after calcination and reduction treatments using a Kratos AXIS Ultra DLD photoelectron spectrometer using a monochromatic Al Kα source operating at 150W. Charge compensation was accomplished using low energy electrons. Standard operating conditions for good charge compensation

were –3.1 V bias voltage, -1.0 V filament voltage and filament current of 2.1 A. Three areas 300x700 micron per sample were analyzed. Survey and high-resolution spectra were acquired at pass energies of 80 eV and 20 eV respectively. All spectral processing was done in CasaXPS. A Shirley background was used for all high-resolution spectra. Sensitivity factors provided by the manufacturer were utilized.

Raman measurements were done using the in Via Raman system, utilizing the 514.5 nm line of an Ar-ion ion laser as well as the 785 nm line of a solid state diode laser. The beam was focused onto the TEM window with a Leica microscope using an x20 objective. Data was collected for the region 100 – 2000 cm^{-1} for 60 seconds, scanned 5 times using a defocused beam of 50% with a laser power of 10% for the 514 nm line (16 mW) and 1% for the 785 nm line (100 mW). 3 separate spectra were obtained for each sample and then averaged to obtain the final spectrum used for analysis. Wire Version 3.2 software was used for data capturing and instrument control. The Raman band of pure Si was measured before data accumulation commenced for calibration purposes.

6.3 Results

6.3.1 Model Catalyst Characterization

Figure6.5 shows images of the model catalysts acquired using a variety of electron microscopes showing how the HAADF imaging mode in the AC-STEM proved to be most useful for this study. The JEOL 2010F was used in the Bright Field (BF) TEM mode for EDX analysis of the sample to acquire compositions of the entire sample and smaller regions of the sample (Figure. 6.6). This allowed us to determine that the sample was uniform in composition; however we learned that when the beam was focused on individual

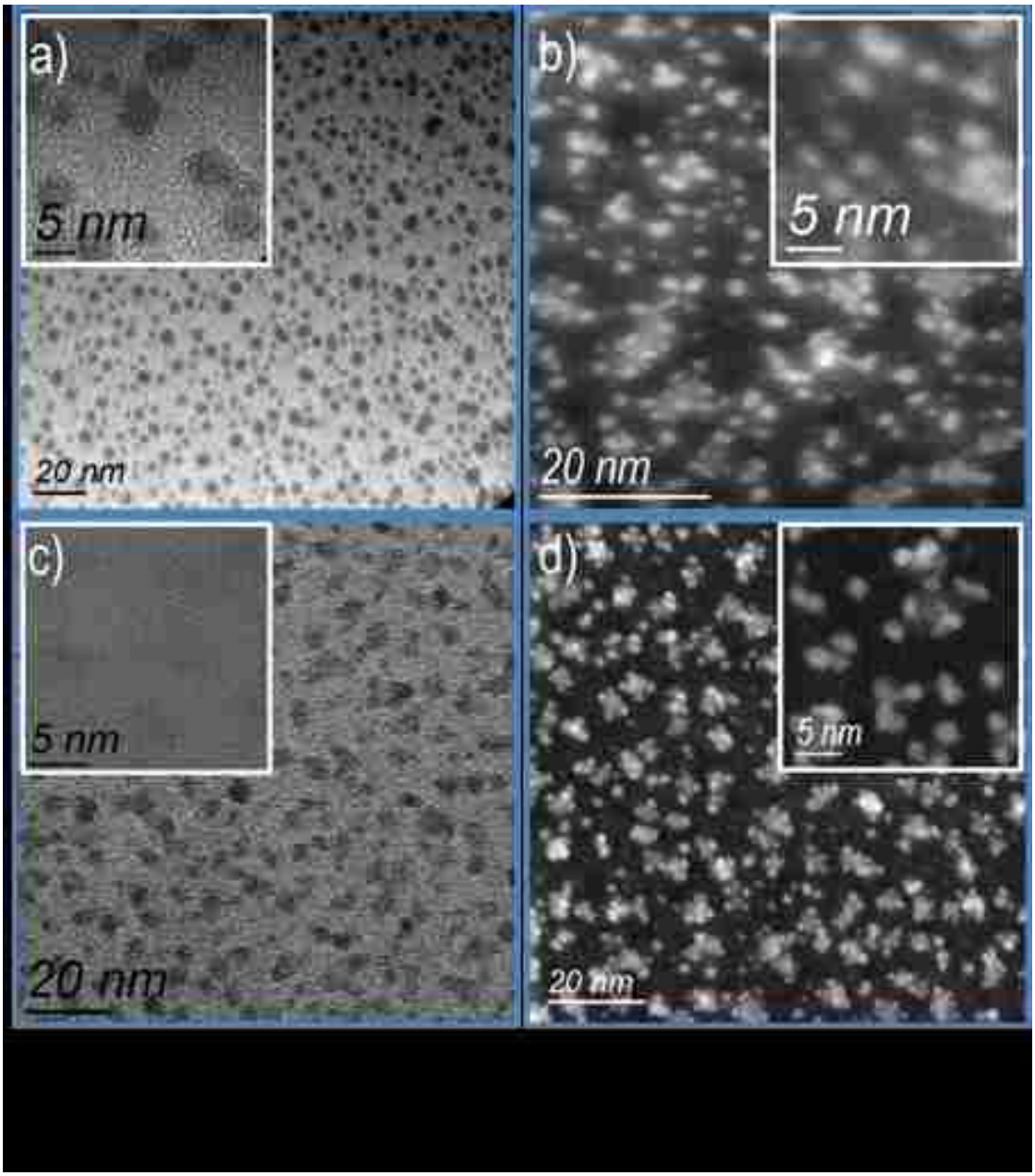

nanoparticles, we saw a definite loss of Zn, with increasing Pd/Zn ratio as the beam was focused on smaller regions of the sample (Figure6.6). Figure. 6.5b shows the HAADF image acquired on this same microscope, showing faint contrast suggesting

dispersed ZnO on the support, but which could not be confirmed with this microscope due to limited resolution. We also examined the same sample in an aberration corrected (AC) TEM

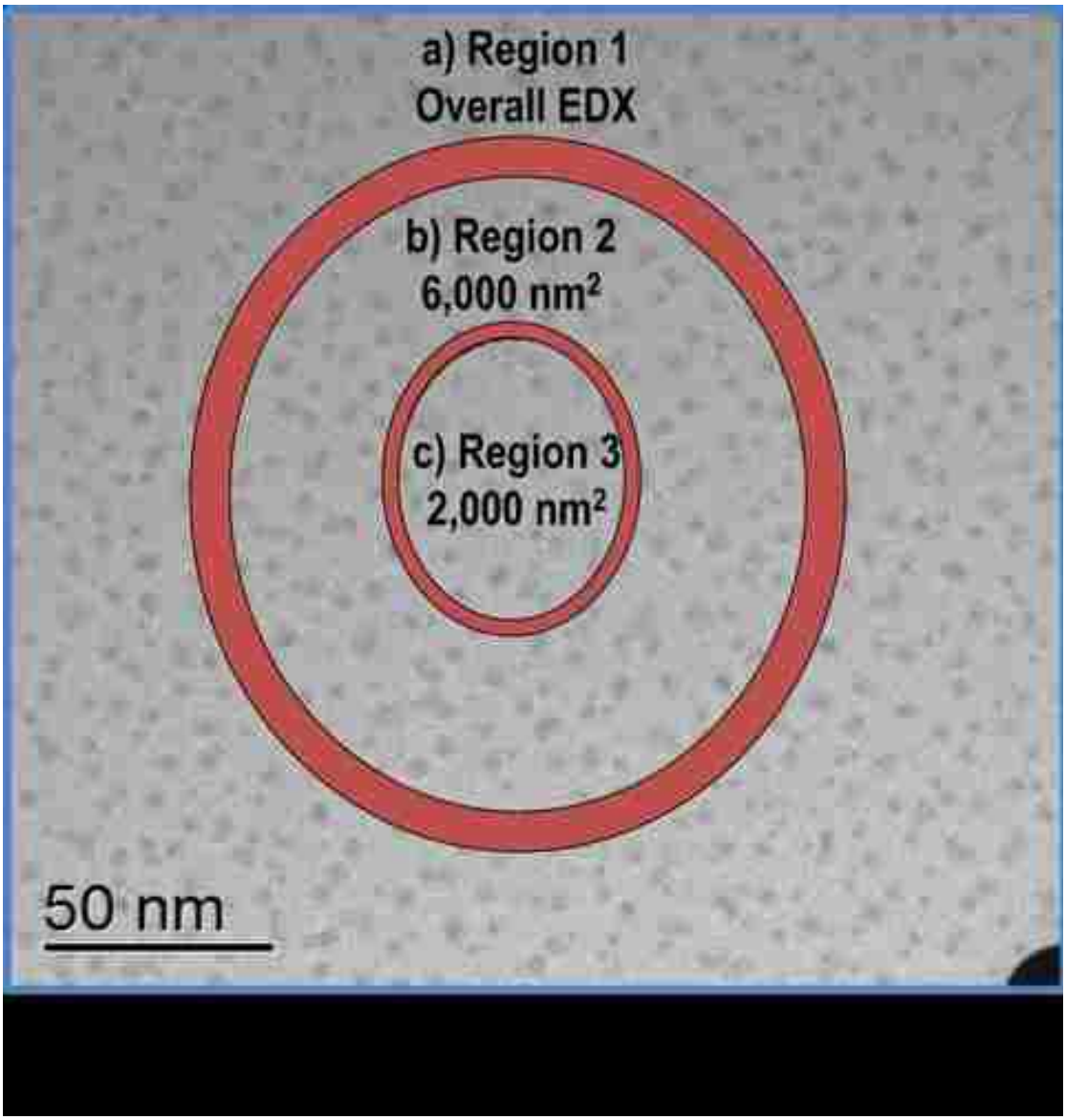

with an image corrector, the Titan 80-300 from FEI (Figure. 6.5c). While this microscope provides excellent lattice resolution, the contrast of the support is so strong as to obscure much of the information. Figure6.5d shows the image obtained with the JEOL 200 F ARM in the probe-corrected mode. The probe size is less than 0.8 Å allowing atomic resolution images with very high contrast. All aspects of the sample can be clearly seen, including the plate like structures of ZnO that are formed when the catalyst is reduced at 100˚C in H_2. The specific microscope we used was not equipped with a large area EDX detector, so we

performed mapping using a Tecnai Ossiris microscope that is equipped with a set of four x-ray detectors providing improved efficiency for collecting x-rays. The combination of a probe corrected STEM with efficient EDX analysis was found to be most effective for the study of these bimetallic catalysts.

6.3.2 Pd-Zn/SiO_2 calcined 450 °C

Figure6.7 shows the HAADF TEM image along with an x-ray fluorescence map acquired via EDX of the sample calcined at 450˚C for 1 hour in flowing 100 sccm in air. The EDX shows an overall concentration of 56.6 atomic (at) % Pd and 43.4 at % Zn which is in agreement with the XPS derived surface concentration of 56.5 at% Pd (Pd 3d) and 43.5 at% Zn (Zn 2p). These concentrations are well within the β1-PdZn phase as defined in the bulk PdZn phase diagram [40, 51] EDX compositional mapping of this sample reveals well defined particles that are Pd rich (red). These nanoparticles also contain Zn (green) but we also see significant amounts of Zn with small amounts of Pd dispersed as a separate phase on the SiO_2 support, located outside of the well defined, spherical Pd nanoparticles. The crystal structure of these various phases was determined via Aberration corrected HRSTEM using high angle annular dark field (HAADF) imaging. Figure6.8 shows that the atomic scale lattice structure of all of the species on this catalyst can be clearly seen. We see lattice fringes corresponding to ZnO (101) ($d = 2.47Å$) in agreement with EDX compositional mapping. The central area of this bright patch, which consists of both Pd and Zn, can be attributed to a mixed Pd/Zn oxide we will now refer to as (Pd,Zn)O seen previously. This mixed oxide has the structure of tetragonal PdO, but it contains Zn isomorphously substituted into Pd sites. In this image, we see the mixed oxide oriented along the [010] zone axis with

the (101) and (202) planes visible. By using the combined information from EDX mapping

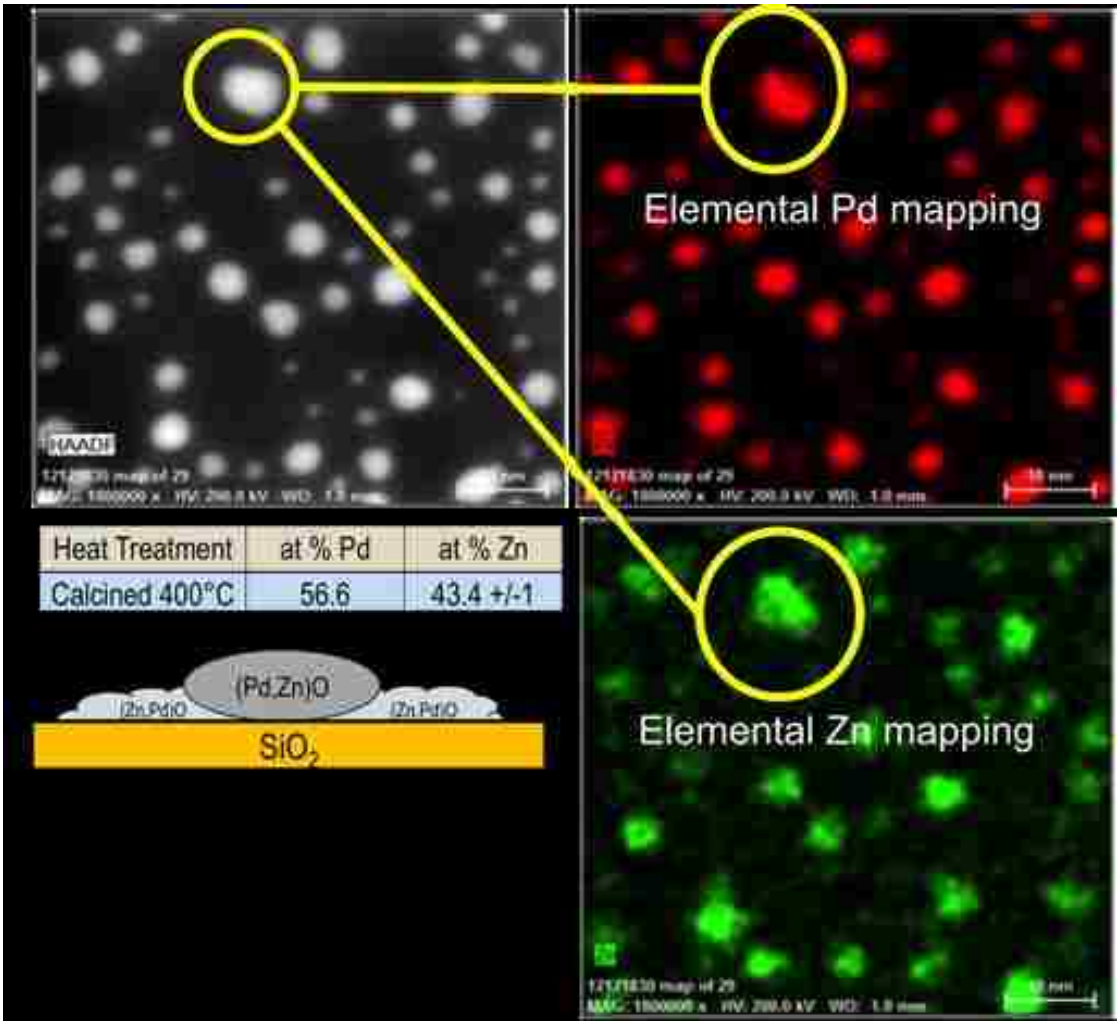

and HAADF imaging, we can infer that the sample after calcination contains the (Pd,Zn)O mixed oxide surrounded by ZnO with slight amounts of Pd incorporated into the ZnO lattice which we will now refer to as (Zn,Pd)O. Pd has been known to isomorphously substitute itself within ZnO at small concentrations [52]. This remaining Zn in the (Zn,Pd)O represents the excess Zn that could not be accommodated within the PdO lattice. Based on the EDS analysis of individual nanoparticles and the analysis of the aerosol derived mixed oxide, we conclude that the Pd-rich mixed oxide has a composition 70 at % Pd and 30 at% Zn.

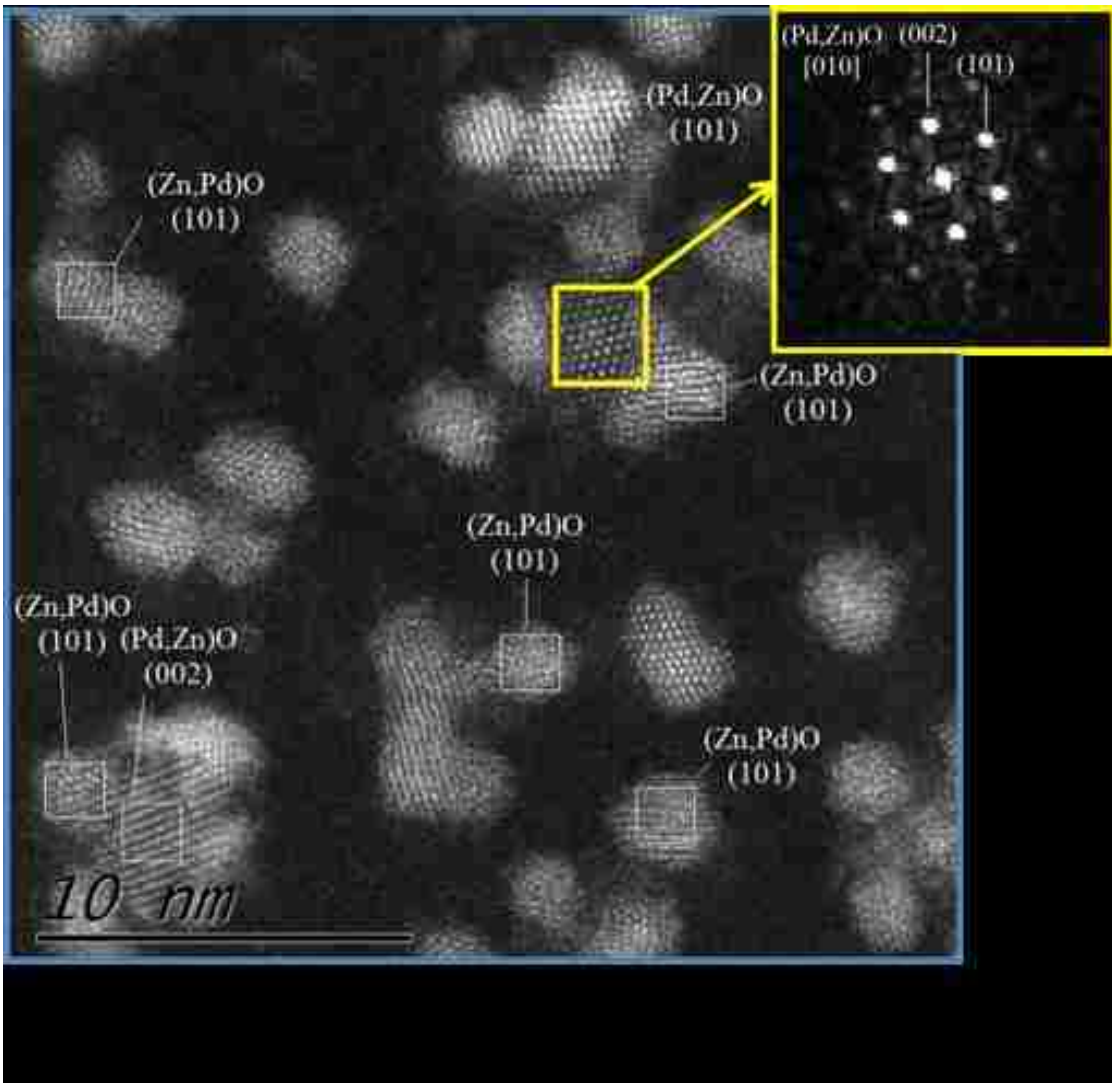

We also performed micro Raman spectroscopy to investigate the nature of the oxide. Figure6.9 shows that the prominent peak of PdO is clearly seen in this spectrum. In related work, we have learnt with the aerosol derived mixed oxide that the PdO Raman band decreases in intensity after isomorphous substitution of Zn for Pd. The intense ZnO Raman band is lost as soon as even small amounts of Pd are incorporated into the ZnO lattice. Hence, the Raman spectrum is consistent with the TEM analysis and provides further corroboration of the nature of the oxide species in this model catalyst.

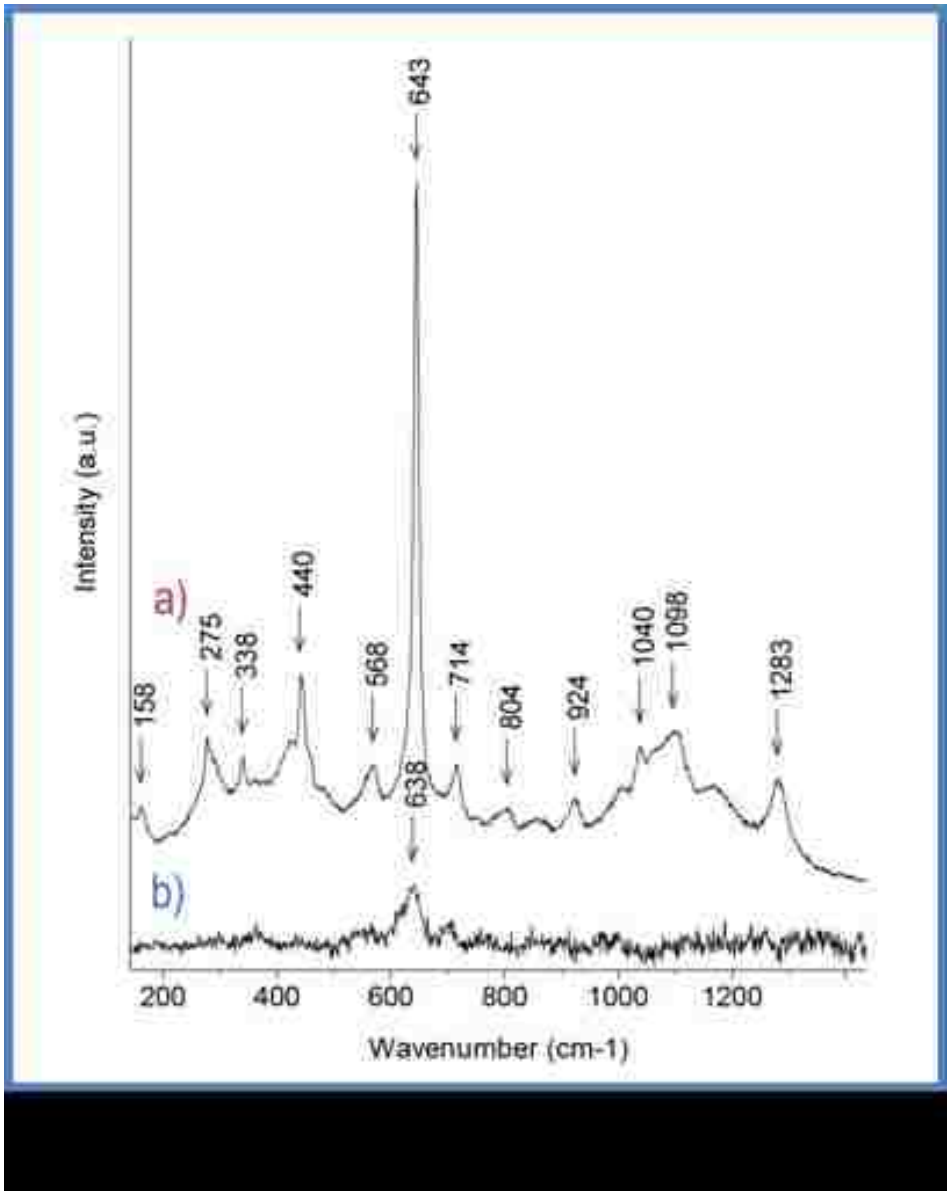

6.3.3 Pd-Zn/SiO_2 reduced in H_2

Figure 6.10 shows that the sample after reduction at 100˚C for 15 minutes under 100 sccm of flowing 7% H_2 93% N_2 at 100˚C. The sample maintains its initial concentration of Pd and Zn and the mixed oxide nanoparticles get reduced to metallic Pd with Zn alloyed within the lattice. Since the structure is fcc, we identify this phase as α-Pd. This α-Pd was shown in

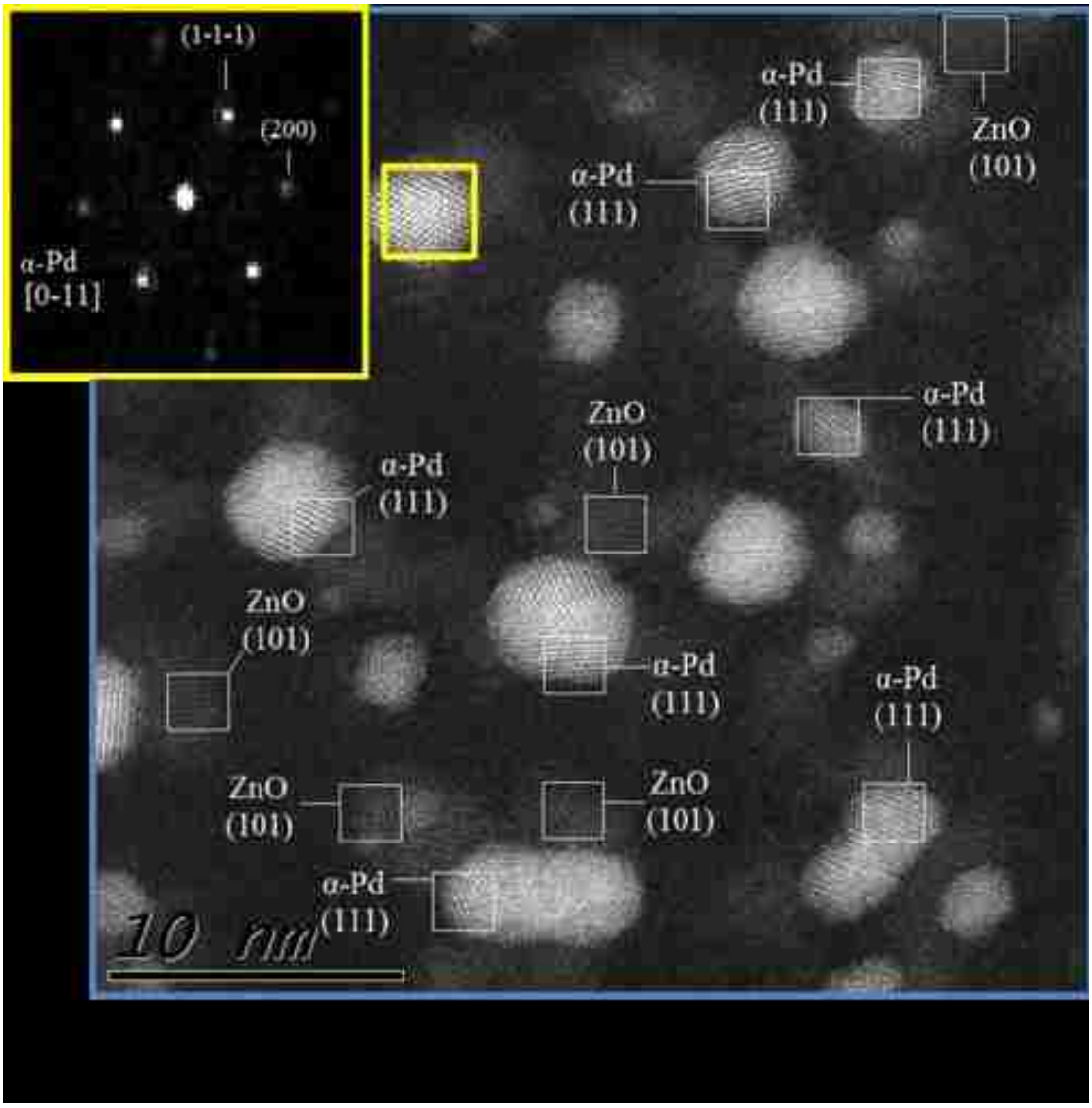

previous work to have a higher reactivity than Pd for MSR but a selectivity that resembles Pd, producing only CO and no CO_2 [13].

Figure 6.11 demonstrates the change in morphology of the ZnO throughout the support from the calcined 400˚C sample to the reduced 100˚C sample exposed to the same calcination conditions. The change in morphology is apparently caused by the low temperature reduction of Pd to form separate Pd fcc nanoparticles. Loss of the Pd leads to

expulsion of the Pd from the ZnO lattice. A similar change in the ZnO morphology was seen via aerosol routes, which will be documented in a future publication.

After increasing the temperature of reduction to 300˚C we see the initial formation of tetragonal β1-PdZn phase (Figure6.12). HRSTEM cross fringe analysis was essential when distinguishing between α-Pd and β1-PdZn crystallites due to their similar d-spacings. The

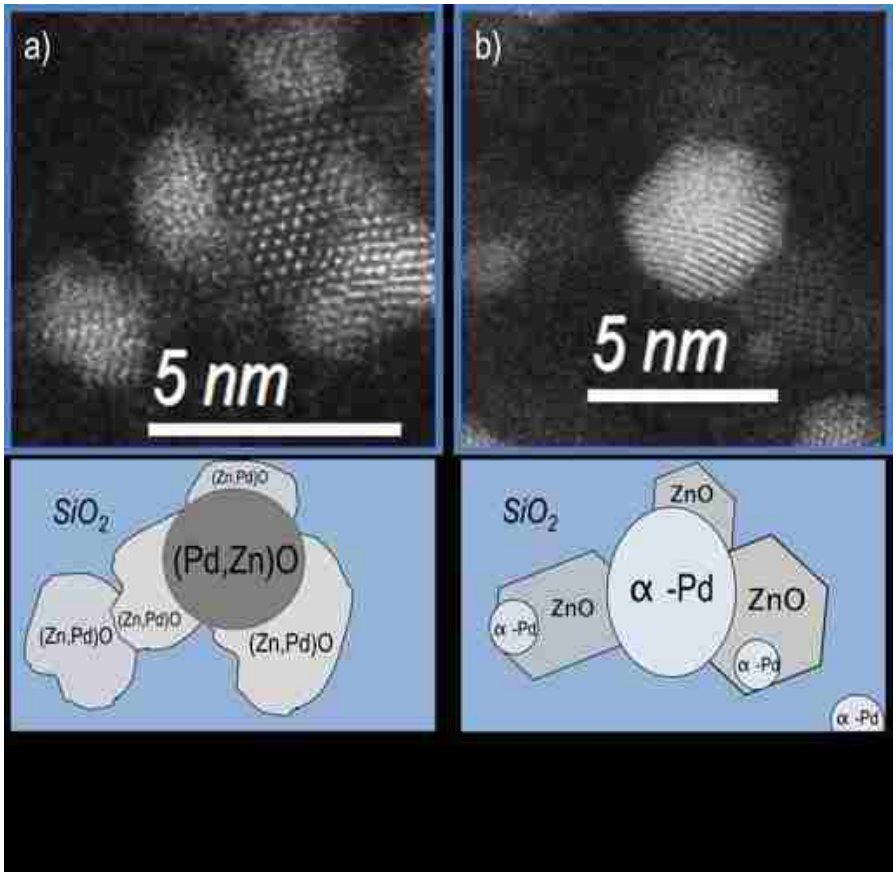

PdZn crystallite in Figure 6.12 are oriented along the [1-11] zone axis with exposed planes of (110) *d = 2.05 Å* and (011) *d = 2.19 Å*. We also see coexistence of α-Pd nanoparticles long with the β1-PdZn. After higher reduction temperatures of 400˚C for 15 minutes in flowing 7% H_2 93% N_2, EDX compositional mapping of the sample (Figure 6.13) shows that the dispersed ZnO has disappeared and all of the Zn is located in conjunction with the Pd

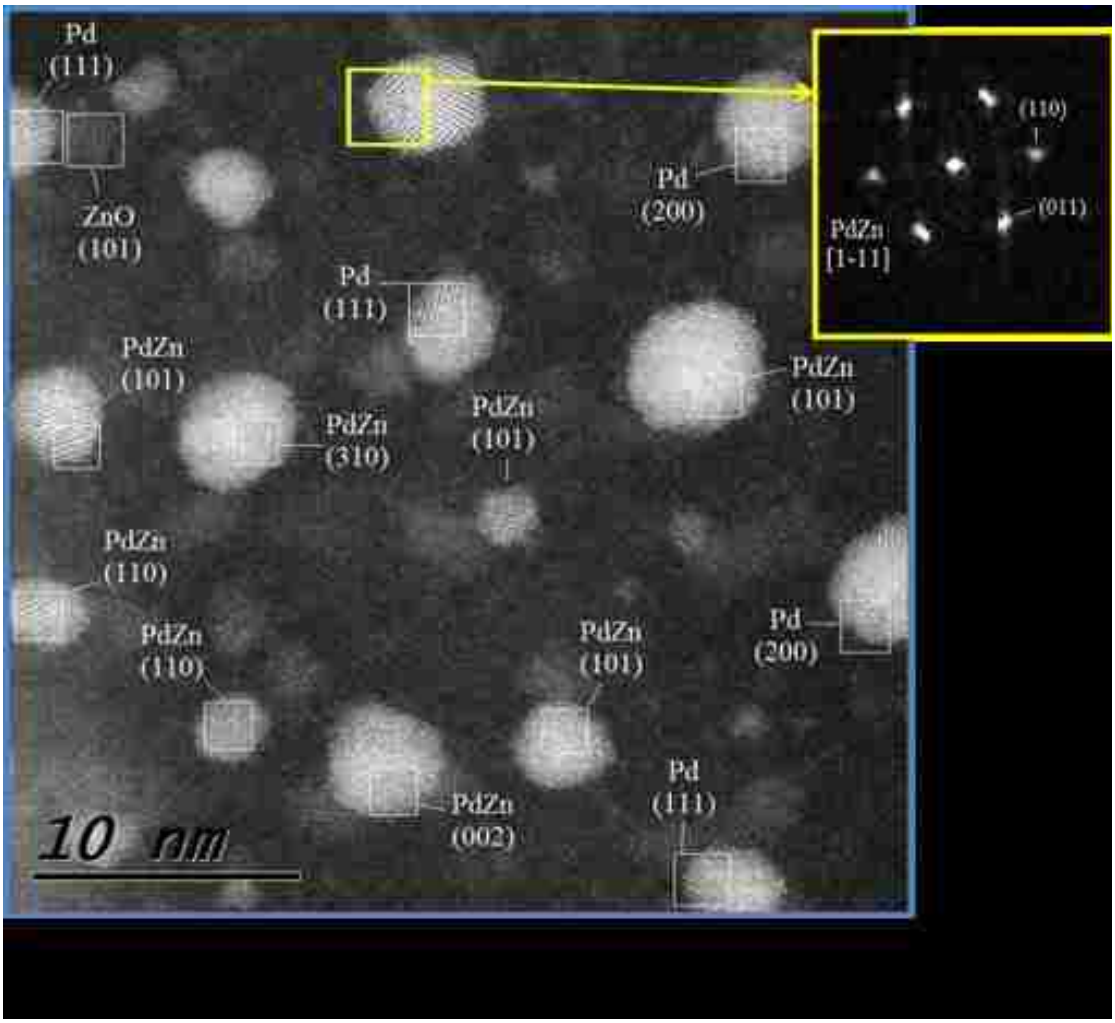

particles, indicating the nearly complete transformation into intermetallic β1-PdZn.

The alloy formation was also confirmed by XPS (Figure6.14). XPS analysis reveals an initial Pd $3d_{5/2}$ core peak close to 337 eV indicating the existence of Pd oxide after calcination [6]. A decrease in the Pd $3d_{5/2}$ energy to ~335 eV is seen after reduction at 100˚C. This decrease in binding energy can be attributed to formation of Pd^0 species. Further reduction leads to the formation of the intermetallic with the final energy shift of 0.7-0.6 eV

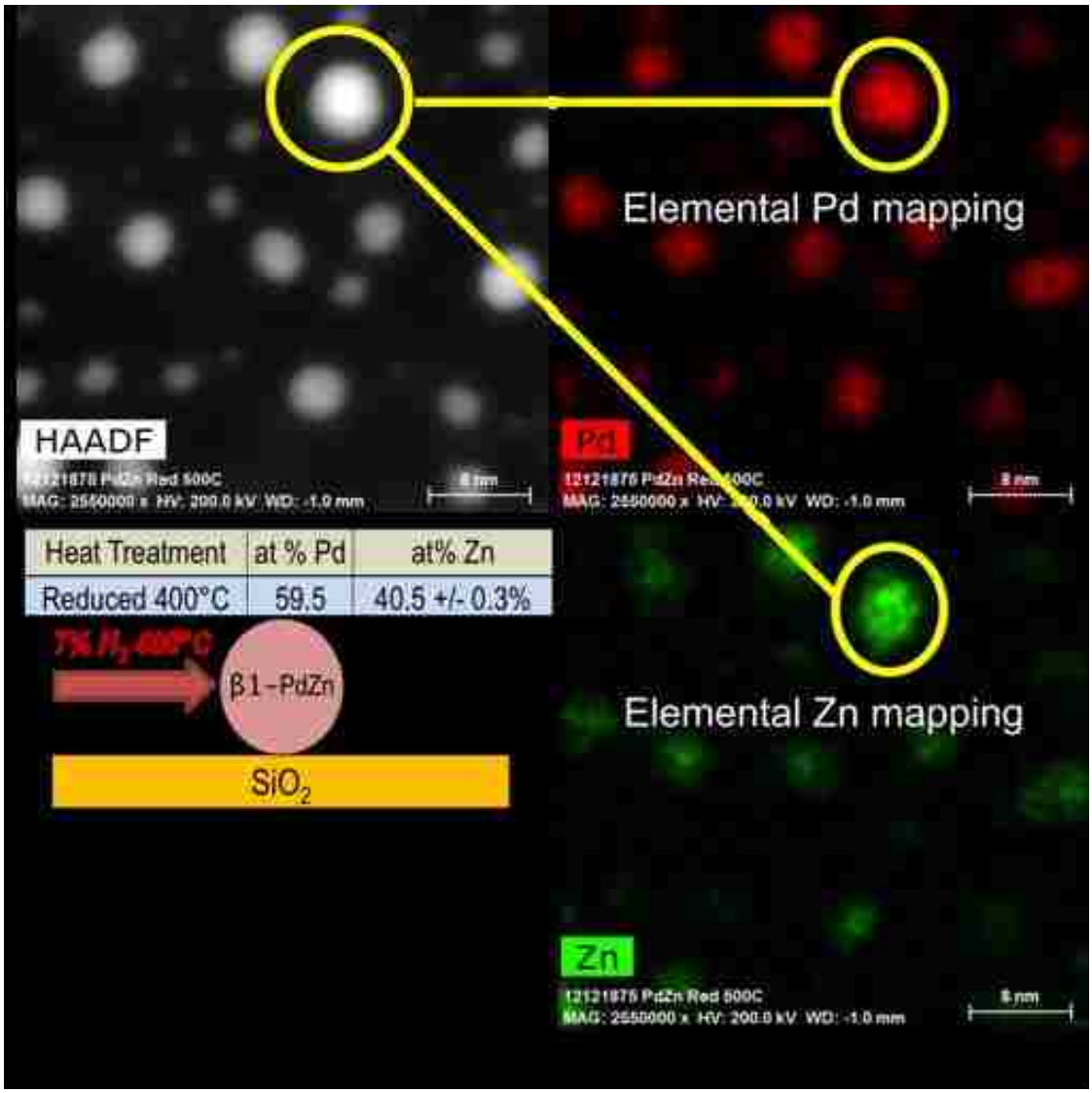

after reduction at 400˚C [6, 53].

After a reduction of 500˚C, the overall EDX Zn concentration decreases to 34.3 at% from the initial 43.4 at %. XPS gives a similar concentration of 34.5 at% Zn (2p). Investigation of the sample using HRSTEM reveals the co-existence of the thermodynamically stable Pd_2Zn bulk phase that has not previously been seen in nanoparticles along with β1-PdZn. Pd_2Zn orthorhombic crystallites can be seen (Figure 6.15) on their [361] zone axis with the exposed planes of (2-10) $d = 2.52$ *Å* and (10-3) $d = 2.32$ *Å*. The loss of Zn concentration and formation of Pd_2Zn is an indication of the decreased

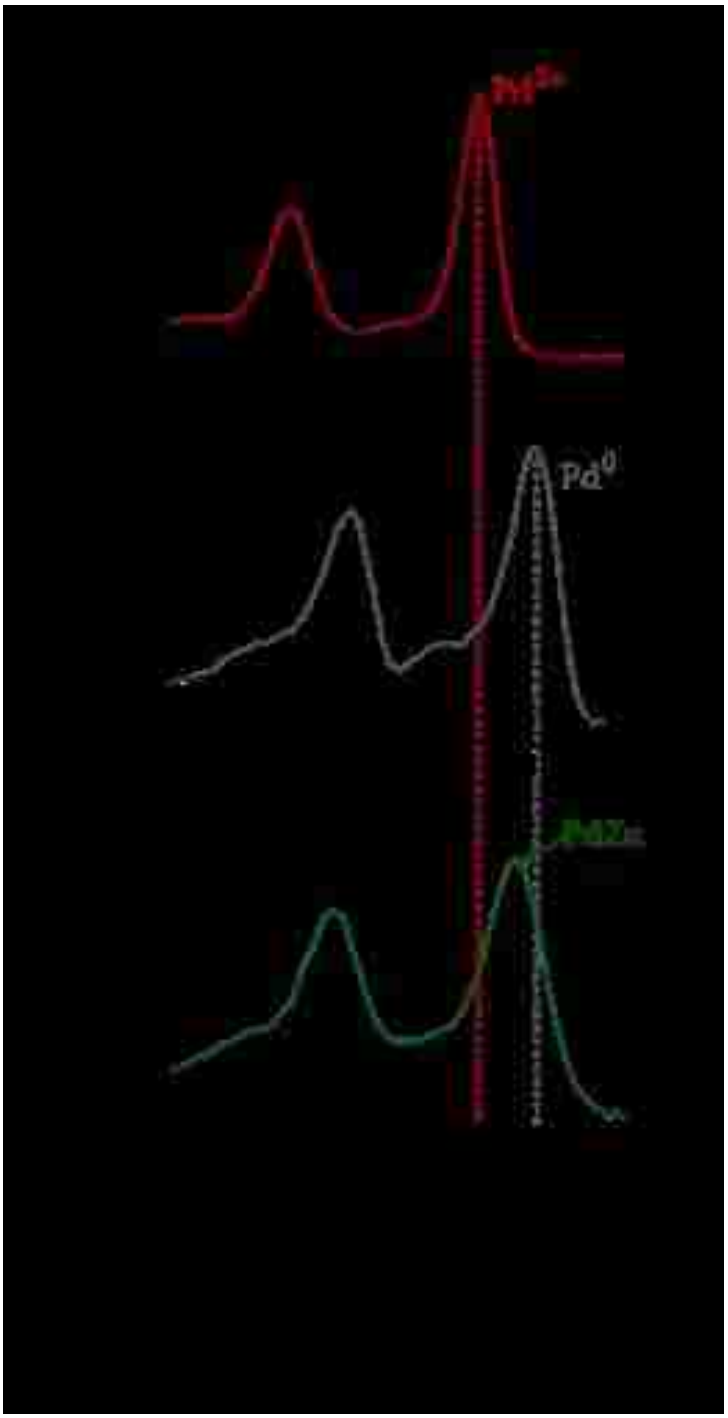

stability of the β1-tetragonal PdZn phase at high temperatures. After further reduction at 600˚C the model catalyst once again shows further loss of Zn leading to formation of the α-Pd phase.

6.4 Discussion

The model catalysts provide unique insights into the phase transformations in the Pd-Zn system. The overall process is depicted schematically in Scheme 6.1. The transformations indicate that when prepared from Pd and Zn precursors, the sample consists of two phases, a Pd-rich oxide that adopts the tetragonal lattice of PdO, and a Zn-rich oxide that has the hexagonal wurtzite structure of ZnO. The Raman spectrum shows that the signal from the model catalyst sample is dominated by the PdO spectrum, and this is consistent with literature reports that show a loss of Raman intensity from the ZnO as soon as Pd is substituted within the lattice [52]. While Pd,Zn oxide samples have been prepared via co-impregnation, the nature of the oxide phase has not been previously characterized.

As the mixed oxide is reduced, the model catalysts show that the Pd gets reduced very easily, and segregates into well-defined nanoparticles of fcc Pd. However, small amounts of Zn are incorporated into the Pd lattice, indicating this the $PdZn_{\alpha}$ phase, involving a solid solution of Zn in fcc Pd. With the Pd lost from the Pd-rich mixed oxide, the ZnO crystallizes into the hexagonal ZnO lattice, forming sheet-like structures that provide very low contrast in the HAADF STEM images. This first step in the reduction process would be very difficult to study without the improved contrast and resolution offered by the model catalysts. As the catalyst is reduced at higher temperatures, the Pd serves as the source of atomic hydrogen, leading to reduction of the ZnO in close proximity, eventually forming the PdZn intermetallic phase. Our results show that the formation of this intermetallic is not complete by 300°C and the sample shows co-existence of the $PdZn_{\alpha}$ (α-Pd) and the $PdZn_{\beta 1}$ phases. A number of authors demonstrated that the Pd/ZnO system was active after reduction at 250˚C [13, 19] however, they also noted that the selectivity selectivity towards CO_2 was low. XRD peaks

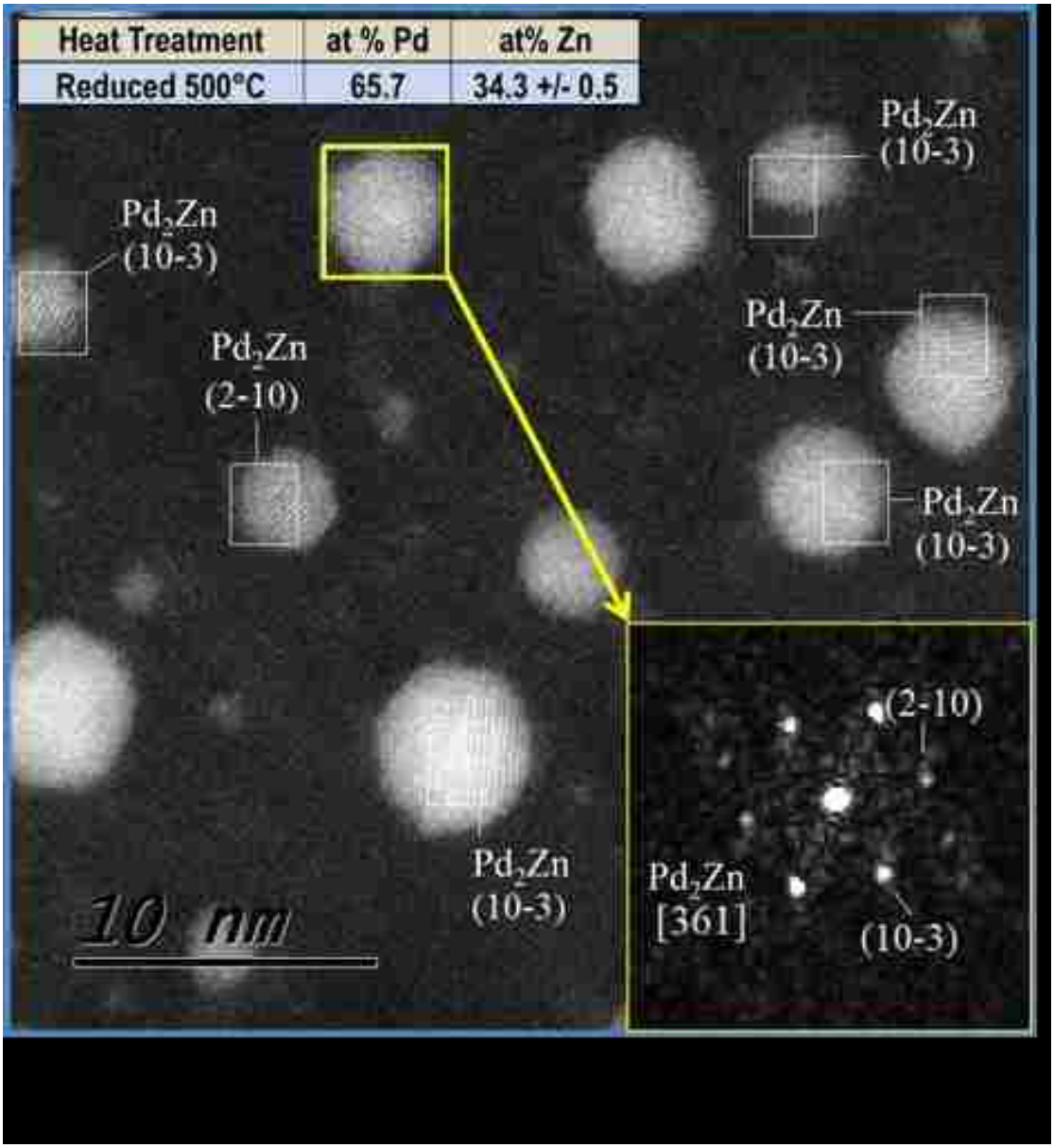

used in these studies were inconclusive to the phases present on their supported catalyst. The model catalyst samples allow us to assign the low selectivity to the presence of α-PdZn which we showed in previous work as leading to CO formation, while β1-PdZn leading to formation of only CO_2 [54]. As the model catalysts are reduced at higher temperatures, we see a loss of Zn evident from EDX analysis, and the formation of the Pd_2Zn phase after treatment at 500 °C. Loss of MSR activity has been observed previously in supported PdZn catalysts where it was suggested to be caused by loss of Zn [19]. They noted loss of catalytic

activity and selectivity of their catalysts after high temperature reduction of 500˚C on their $PdZn/Al_2O_3$. Further studies will involve reacting an alumina supported PdZn catalyst synthesized with acetate precursors along with reaction of single-phase Pd_2Zn catalysts to derive specific reactivity for this phase which has not yet been reported in the literature on PdZn catalysts. This model catalyst however clearly demonstrates the mobility and the volatility of Zn in the PdZn system.

6.6 Conclusion

This work presents demonstrates a simple platform for the study of complex multimetallic catalysts. The samples can be prepared using liquid phase precursors, and by using spin coating, we can generate uniformly sized nanoparticles. The use of the silica as a TEM support combined with aberration corrected HRSTEM, EDX, XPS and Raman allow for a very detailed look into PdZn nanoparticle formation from (Pd,Zn)O → α-Pd → β1-PdZn → Pd_2Zn and back to α-Pd. The work shows that despite starting with a mixed oxide of PdO and ZnO, the first step involves the reduction of the Pd to fcc Pd which then serves the source of atomic hydrogen to reduce ZnO and release metallic Zn that can form the intermetallic phase. The findings provide insight into the role of reduction temperature, showing that nanoparticles of the desired tetragonal PdZn phase can be formed at relatively low temperatures on suitable supports, while in the case of ZnO as a support we see the growth of even larger particles, leading to a loss of reactivity. This general platform is versatile since the model catalysts can be treated just like conventional heterogeneous catalysts in terms of the temperatures used for oxidation and reduction. The low background

of the thin Si_3N_4 film provides detailed atomic scale insights into the phase evolution of these catalysts.

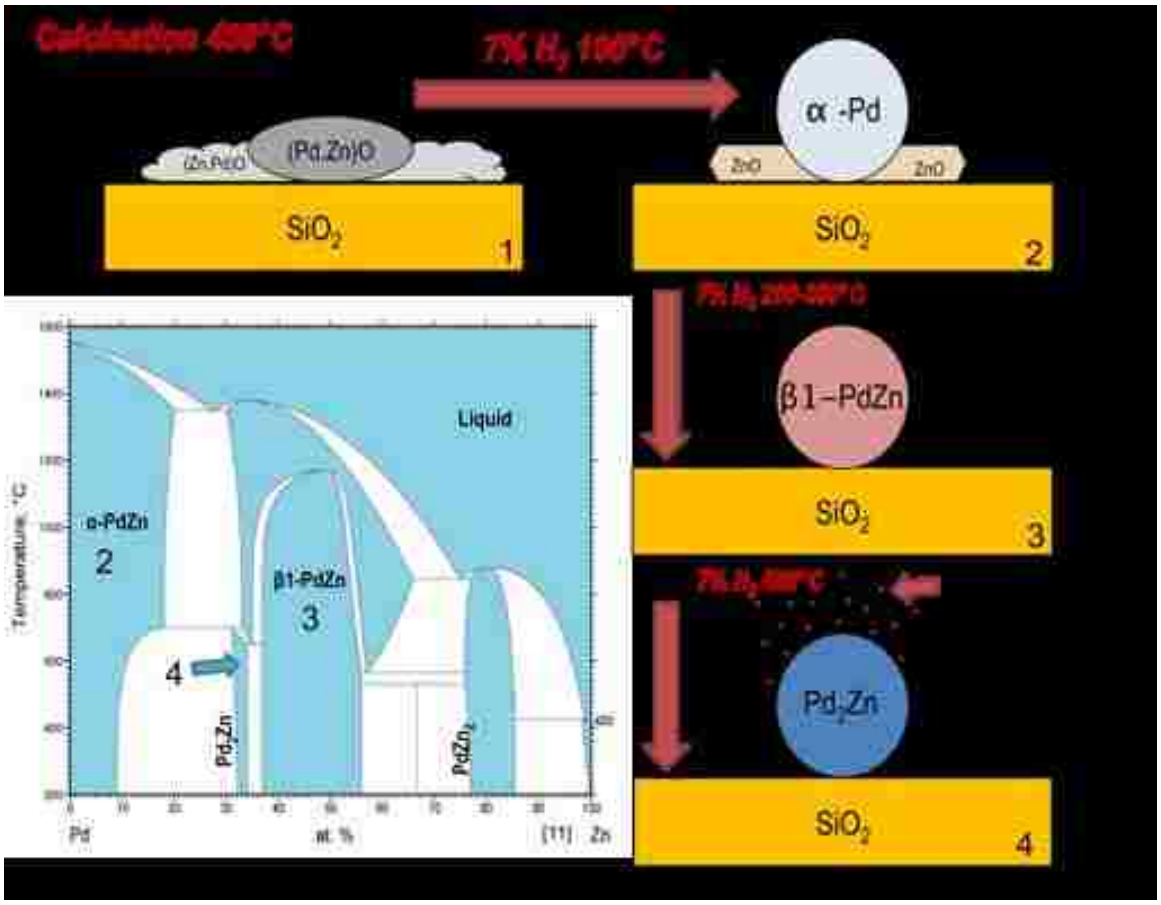

Chapter 7.

Active site investigation into PdZn phase transformations for MSR:

Preliminary and future work: 1 wt% Pd/ZnO

7.1 Introduction

Active sites on catalysts generally behave differently under working conditions. For bimetallic systems the concentration on the surface may differ greatly than the concentration in the bulk. Thus in order to understand the dynamic nature of the catalysts the catalysts itself must be studied in a dynamic manner [55].

These dynamic properties are no stranger to the PdZn system. The active surface of PdZn has been known to change after various reduction and oxidative treatments, which can have an affect on overall activity [13, 19]. Supported PdZn/ZnO catalysts have been known to sinter at high temperatures leading to an increase in overall particle size however a number of studies have demonstrated that this change in particle size has no affect on the overall activity of the catalyst [6, 13, 56]. This leveled activity with increased crystallite size calls into question the implied change of turn over frequency or structural sensitivity for the PdZn system. Iwasa's [6] fundamental work noted a leveled conversion after reduction at 420˚C but further documented an increase of particle size via XRD. Karim *et al.* [13] also saw this leveled conversion with increase in particle size but described this change in arbitrary units, (% conversion/ weight of catalyst) units that do not describe the rate per active site or turn over frequency (TOF). Usually structure sensitivity is limited to nanoparticles less than 10 nm in size however these experiments suggest otherwise. Unfortunately these current studies

do not allow one to conclude the dependence of structure sensitivity for the PdZn system since neither was successfully able to determine the number of active sites. One reason for this is that measuring active sites via traditional techniques (CO, H_2 chemisorption) for PdZn is difficult since the stoichiometry of CO on Pd is variable and H_2 has been known to react with Pd forming Pd hydride [18]. However recently, CO oxidation has been proposed as an ideal probe reaction for the study of active sites and surfaces in heterogeneous catalysis [57]. Currently in our group CO oxidation has been used for counting active sites in aerosol-derived bimetallics [18, 58]. These studies used CO oxidation as an *in-situ* probe reaction to count the number of active Pd sites. Halevi *et al*. [18] were able to apply the TOF of CO oxidation and use it to determine the TOF for MSR. Currently, however, the challenge is to apply this method to supported PdZn catalysts where the surface lacks uniformity. This current chapter presents the initial work done to determine the TOF values for supported PdZn catalysts and proposes the future work and calculations that must be done to determine the change of TOF as a function of *in-stu* PdZn phase transformation for MSR.

7.2 Experimental

7.2.1 CO oxidation

CO oxidation was first performed on a pure Pd metal powder (Sigma Aldrich CAS #7440-05-3) obtained from Sigma Aldrich and was used as a standard benchmark for the CO oxidation test reactions according to the method described by Johnson *et al*. [58] 40.8 mg of the reference Pd powder was calcined in air at 350˚C for 3 hours and then reduced in flowing 7% H_2 for 4 hours. The surface area of the Pd sample was determined by N_2 adsorption using the BET method (5 m^2/gram). By using the average number of Pd atoms per unit surface area for the low index plane of Pd (1.26 surface atoms per 10^{-19} m^2) we can estimate the number

of Pd atoms per gram of sample for the pure Pd powder. Estimating the number of Pd sites we were able to determine the TOF expressed as moles of CO_2 produced per mole of surface Pd per second. CO oxidation was also performed on 40 mg of the 1wt% Pd/ZnO sample described in previous chapters.

The effluent of the reactor was analyzed using a Varian CP 3800 gas chromatograph (GC) equipped with a Porapak Q column and a molecular mole sieve. The GC operated in Series/Bypass mode for CO oxidation with He as a carrier gas. For CO oxidation 1.5 sccm CO, 0.8 sccm O_2 and 70 sccm as an inert feed (He) gas were fed into the catalyst bed. The conversion of CO was determined by measuring the effluent for CO, O_2 and CO_2 while using the response factor for CO to CO_2. The GC was programmed to sample the stream every 7.08 minutes. The first injection was taken after 10 minutes on stream. The 1wt% Pd/ZnO sample was reduced *in-situ* in 7% flowing H_2 for 4 hours (100, 200, 300, 400, 500˚C) and subjected to CO oxidation at 193˚C to monitor the change in conversion with respect to time and H_2 treatment.

7.2.2 Coupled MSR and CO oxidation

The in house MSR/CO oxidation system allows for simultaneous measurements of CO oxidation and MSR. For the initial TOF phase transformation experiments 54.8 mg of the 1wt% Pd/ZnO catalysts was reduced *in-situ* under 7% Flowing H_2 for 2 hours at (300, 400 and 500˚C). Immediately following reduction the 1wt% Pd/ZnO was cooled to 258˚C under He. The analysis of the gas phase species CO_2, CO, CH_3OH and H_2O along with a carbon balance allowed the methanol conversion and CO_2 selectivity to be calculated. The GC operated in Bypass mode with He a carrier gas. The GC was programmed to sample the reactor product every 18 minutes. The catalyst was reacted for 2 hours to get an average

MSR conversion. Immediately following MSR the reactor was cooled to 193˚C for CO

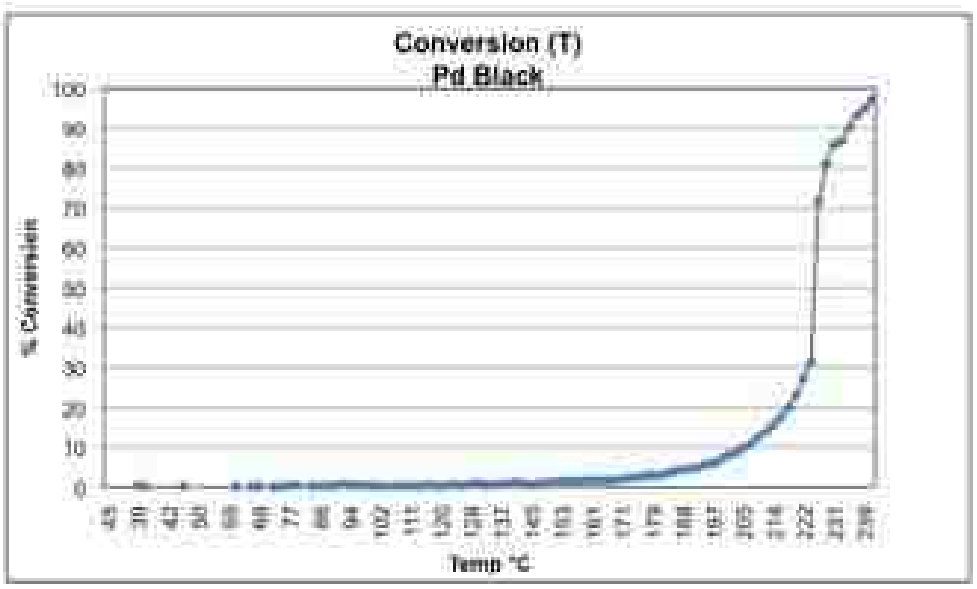

Figure 7.1 Light off curve for CO oxidation for Pd metal powder

oxidation measurements. First injection of the effluent gas was done within 2 minutes to achieve measurement of the PdZn phase and particle size present for that particular MSR run.

7.3 Results

7.3.1 Pd Black CO Oxidation

Pd Black was used as a standard to test the reproducibility of the system and the sample. Figure 7.1 shows the light off curve for Pd metal as a function of temperature. Light off for the Pd metal catalyst begins around 220˚C. The Arrhenius plot for the same sample is seen in Figure7.2. For CO oxidation the activation energy was found to be 79.1 kJ mol^{-1}, which is in close agreement with the values seen by Johnson *et al*. [58] who reported an activation energy of 87 kJ mol^{-1}. The slight difference in activation energy may be attributed to difference in CO/O_2 feed stream ratios. The change in TOF for Pd metal can be seen in Figure 7.3.

7.3.2 Phase Pd/ZnO Isothermal CO oxidation Studies

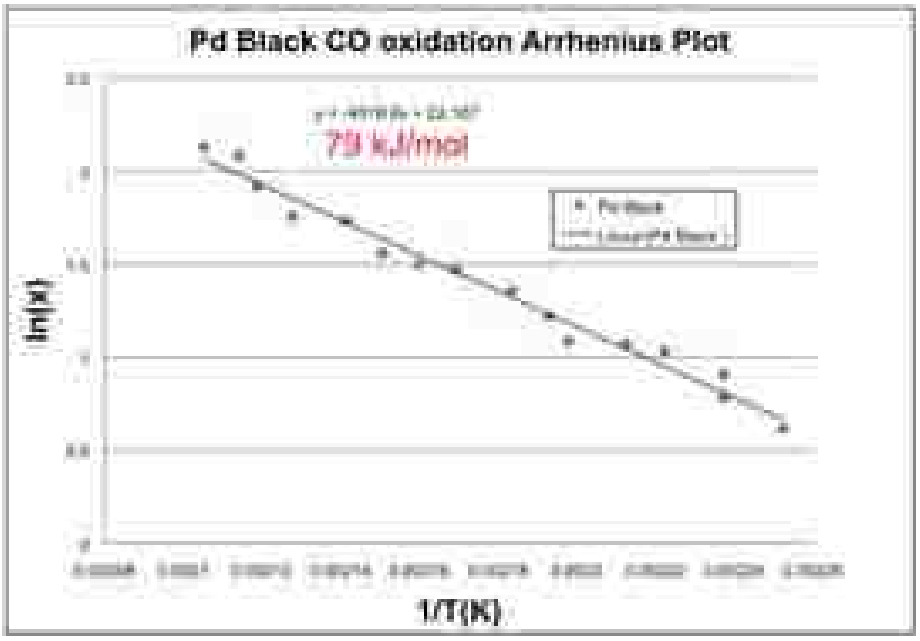

Figure 7.2 Arrhenius Plot of Pd metal for CO oxidation. The activation energy of the sample for CO oxidation was found to 79 kJmol^{-1}

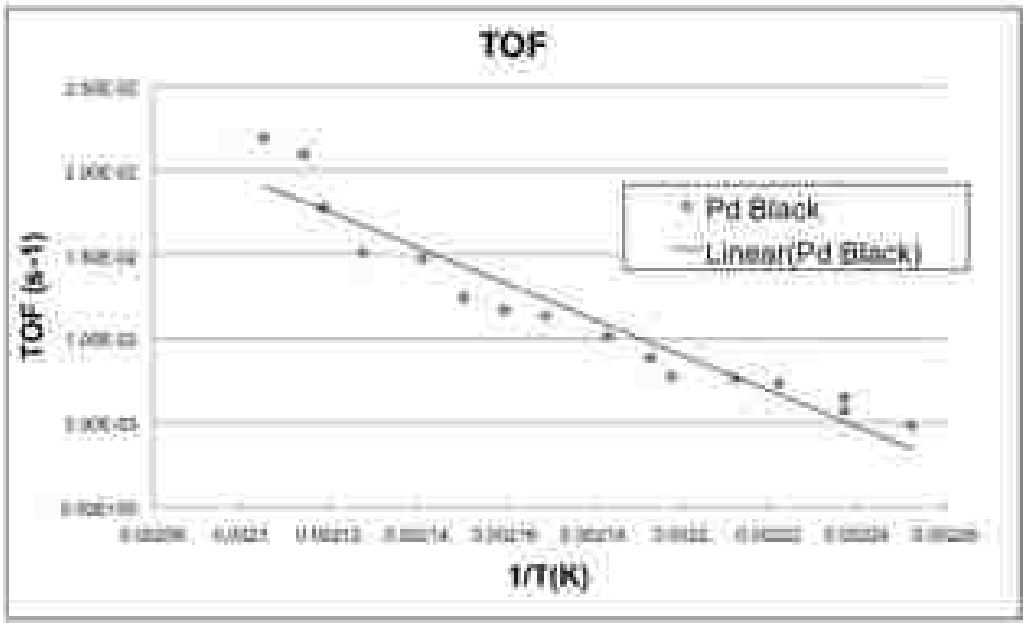

Figure 7.3 Turnover (TOF) frequency for Pd metal for CO oxidation as a function of temperature

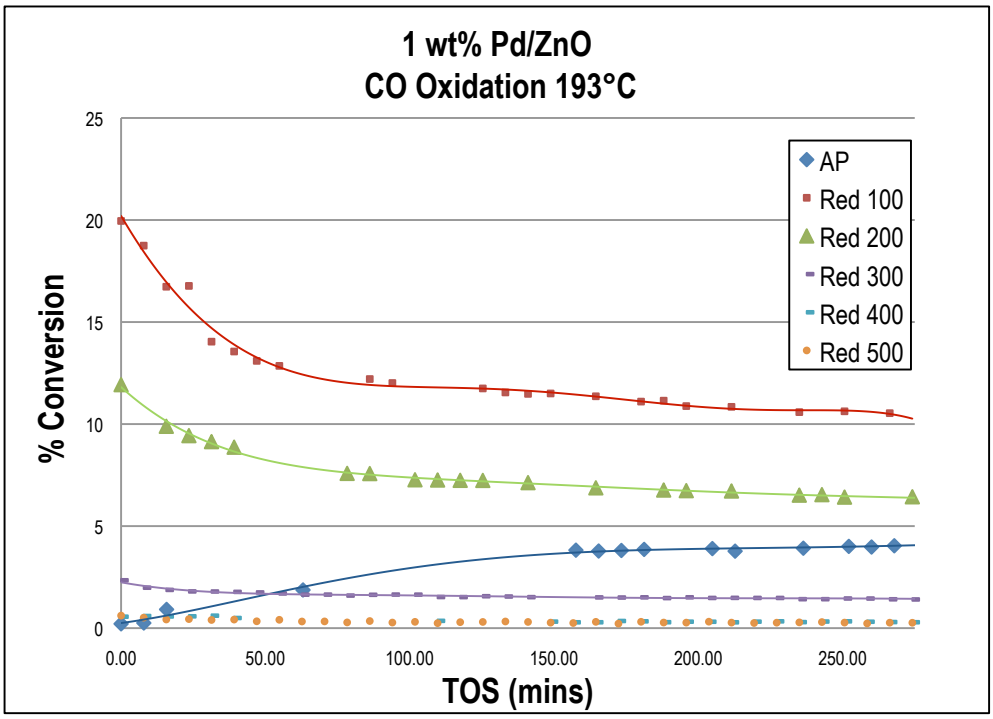

Figure 7.4 CO oxidation over time for 1wt% Pd/ZnO sample after reduction treatments

Previous work demonstrated the decay in activity of PdZn samples after exposure to CO oxidation for supported aerosol catalysts [58], therefore it was of great interest to expose the 1wt% Pd/ZnO samples to isothermal conditions to see if similar phenomena could be observed. These experiments not only allowed us to track the activity change with phase transformation but to also observe the dynamic nature and deactivation of the surface of PdZn for CO oxidation. For this set of experiments the AP (As prepared) 1wt% Pd/ZnO catalysts was exposed to CO oxidation conditions for 250 minutes. After AP exposure the catalyst was reduced at the specified temperature, exposed to CO oxidation conditions and then reduced again. The deactivation over time after each treatment can be seen in Figure7.4. The deactivation over time for the sample reduced at 400˚C can be seen in Figures 7.5.

7.3.3 Coupled MSR and CO oxidation

MSR experiments followed by CO oxidation can be seen in Figure7.6. For these experiments the AP 1 wt% Pd/ZnO was reduced at 300˚C at for 2 hours and then reacted for MSR and then measured for CO oxidation. MSR conversion increased with reduction temperature while CO conversion decreased. The selectivity to CO_2 for MSR remained relatively unchanged for the sample after each reduction temperature.

7.4 Discussion

Figure7.4 clearly demonstrates the dynamic nature of the 1wt% Pd/ZnO catalysts with an increase in reduction temperature. The AP 1 wt% Pd/ZnO sample shows an increase in CO oxidation conversion over time. The initial activity is an indication of the PdO phase of the 1 nm nanoparticles on the ZnO support (Figure7.7). PdO itself is relatively inactive for CO oxidation however for this sample it can implied that the CO reduces the PdO

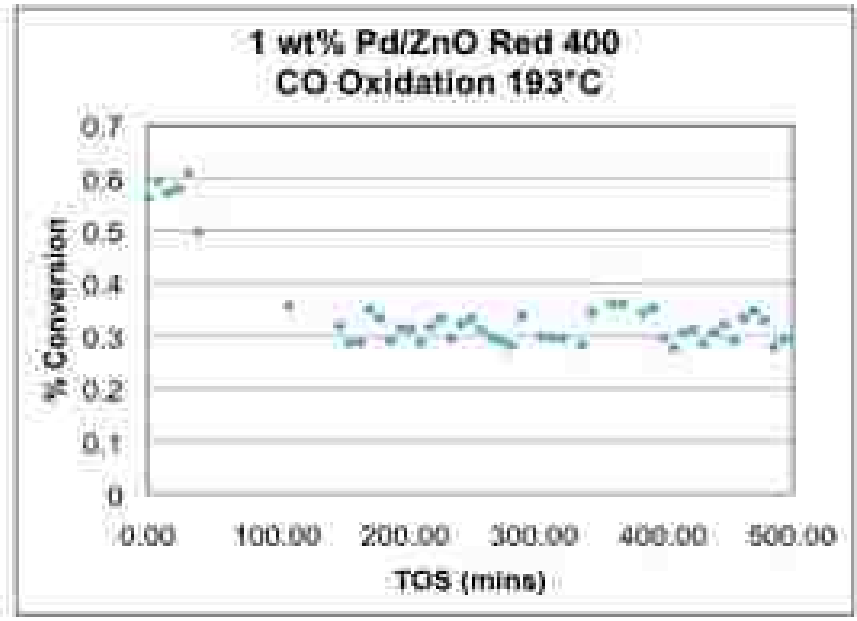

Figure 7.5 CO oxidation for sample reduced at 400˚C

nanoparticles on the surface yielding metallic Pd [59]. This phase transformation can be seen by the gradual increase and leveled conversion since Pd is more active than PdO for CO oxidation. The final activity of the AP sample is the true activity for metallic Pd (~5%). After reduction for 4 hours at 100˚C the initial conversion increases significantly (20%) but steadily declines to 10%. The differences in conversion may be an indication of different phases on the surface of the catalyst. Johnson and coworkers [58] found α-Pd to be more active than pure Pd. This increased activity after 100˚C is an indication of Zn incorporation into the Pd lattice at low reduction temperatures. The catalysts conversion continues to decrease for the 200˚C reduction; the initial CO conversion is 10% and again has a 50%

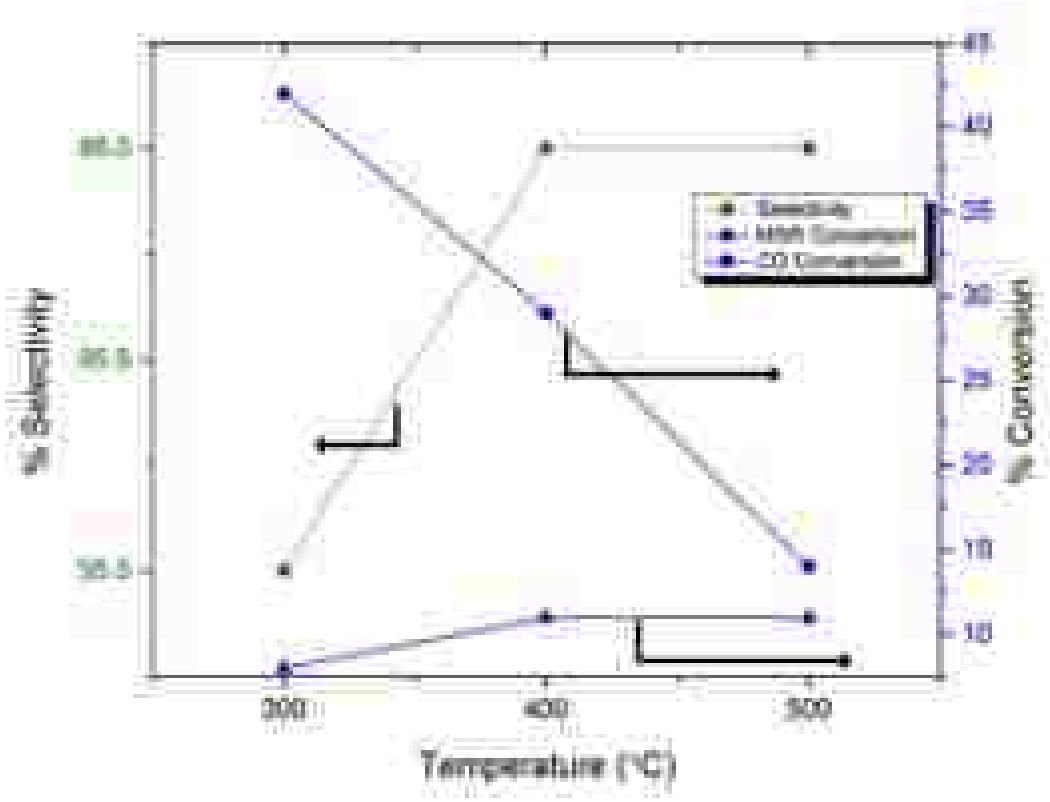

Figure 7.6 Coupled MSR and CO oxidation data. MSR Selectivity to CO_2 (Left). MSR and CO oxidation conversion (Right) and reduction temperature (x-axis)

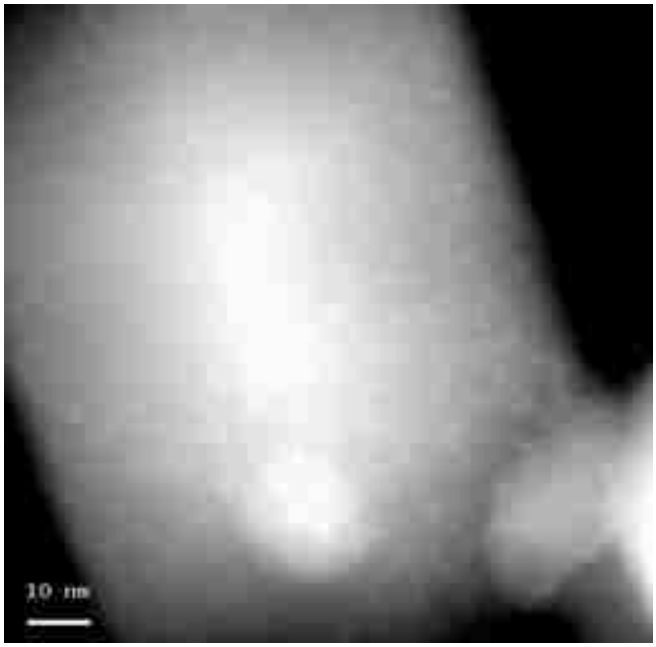

Figure 7.7 STEM image of the AP 1wt% Pd/ZnO sample. STEM shows PdO nanoparticles less than 1 nm in size

decline to 5%. The same is true for the sample reduced at 300˚C. These changes in conversion can be attributed to the phase transformation of α-Pd to β1-PdZn. Johnson *et al.* [58] also confirm this decrease in activity for their phase pure PdZn aerosol powders. Iwasa and coworkers [6] did not see a significant increase in PdZn crystallite size until after reduction temperatures at 400 ˚C, this is reflected in the drastic decrease in conversion for the samples reduced at 400 ˚C (Figure 7.6) and the similar is seen for 500˚C. TEM of sample after reduction and CO oxidation at 500˚C shows large particles demonstrating the decreased surface area leading to the loss in activity of the 1wt% Pd/ZnO (Figure 7.8). The 50% decline in conversion after 100 minutes on stream for each reduced sample can be attributed to the oxidation of Zn leading to the formation of ZnO, this oxidation causes the Pd to lose the enhanced activity it had gained form Zn in the PdZn lattice.

7.7.2 Coupled MSR and CO oxidation

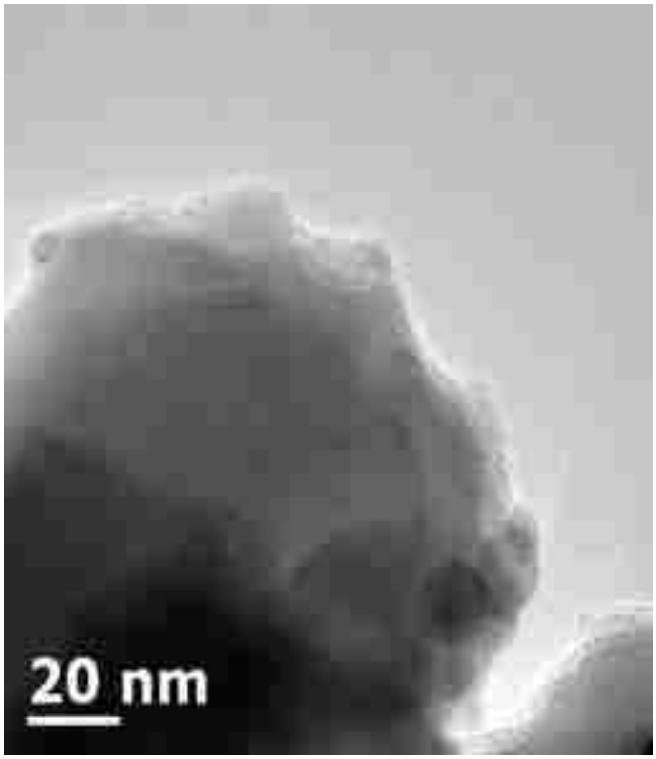

Figure 7.8 TEM image of 1wt% Pd/ZnO sample after reduction treatments. TEM reveals large PdZn nanoparticles on surface of ZnO

This preliminary data follows the trend seen by Iwasa for his fundamental PdZn/ZnO studies [6]. The decreased CO and increased MSR conversion after reduction at high temperatures does indeed imply a change in TOF for the reduced catalyst. In order to determine TOF properly for MSR the number of Pd sites must be determined and compared to the bulk Pd sample. Future work will require the use of XRD and TEM to determine the average crystallite size and phases present in the sample. Once this is known the number Pd sites on the 1wt% Pd/ZnO can be determined from CO oxidation and can be used to determine the TOF for MSR.

7.5 Conclusion

Initial CO oxidation data of the 1wt% Pd/ZnO sample after reduction reflected the various phase changes seen for the PdZn system. The deactivation over time shows similarities between the supported PdZn sample and the aerosol-derived powders. This deactivation of samples can be attributed to the oxidation of Zn to ZnO [58]. The coupled MSR measurements with CO oxidation implies an increase in TOF with increase in crystallite size implied by Iwasa *et al.* [6]. Future work will involve determining the average particle size using XRD and TEM for the PdZn after reduction so that actual TOF values for MSR can be determined.

Chapter 8.

Conclusion and Outlook

With this work I was able to prove the existence of 2 mixed oxides via TEM and SEM for the PdZn aerosol calcined powders, a previously undocumented (Pd,Zn)O and a greater characterized bulk (Zn,Pd)O. The two techniques allowed me to image the distinct phases of different morphologies and with EDX I was able to show the relative Pd concentration in each. This study provided insight into the initial formation of the highly active β1-PdZn that has not been studied in supported PdZn catalysts.

I was able to use spin coating for the first time to understand the complex PdZn bimetallic system. The samples were prepared using liquid precursors, which closely mimic large-scale industrial synthesis techniques. The use of the silica as a TEM support combined with aberration corrected HRSTEM and EDX allowed me to characterize the phase transformation and get a very detailed look into uniform PdZn nanoparticles and their formation from (Pd,Zn)O → α-Pd → β1-PdZn → Pd_2Zn and back to α-Pd. This work showed that one starts with a mixed oxide of PdO and ZnO followed by a step that involves the reduction of the Pd to fcc Pd which then serves the source of atomic hydrogen to reduce ZnO and release metallic Zn that can form the intermetallic phase. The findings provide insight into the role of reduction temperature, showing that nanoparticles of the desired tetragonal PdZn phase can be formed at relatively low temperatures on suitable supports. For the first time I was able to document the formation of Pd_2Zn upon loss of Zn. This is significant since Conant et. *al* [19] was not able to characterize this phase in his alumina supported sample.

.

From my CO oxidation data of the 1wt% Pd/ZnO sample I was able to document the various phase changes seen after reduction for the PdZn system. The deactivation over time shows similarities between the supported PdZn sample and the aerosol-derived powders. For the first time MSR measurements with CO oxidation were ably to quantify increases in TOF with increase in crystallite size. My future work will involve deriving actual TOF values.

My work has shown the complexity of bimetallic systems and also demonstrates how they behave under reaction conditions. Although this work gave me valuable insight, more studies that utilize in-situ techniques must be performed. The challenge remains in understanding the true active surface. This can be accomplished by such experiments that use characterization techniques such as environmental TEM (ETEM), Extended X-ray Absorption Fine Structure (XAFS), Ambient Pressure XPS and In-situ XRD. These future experiments must use multiple if not all to determine the true active nature of the catalyst.

References

1. Kovnir, K., et al., *A new approach to well-defined, stable and site-isolated catalysts.* Science and Technology of Advanced Materials, 2007. **8**(5): p. 420-427.
2. Sinfelt, J.H., *Bimetallic catalysts*. 1987. Medium: X; Size: Pages: 189.
3. Partridge, A., S.L.G. Toussaint, and C.F.J. Flipse, *An AFM investigation of the deposition of nanometer-sized rhodium and copper clusters by spin coating.* Applied Surface Science, 1996. **103**(2): p. 127-140.
4. Li, Y.M. and G.A. Somorjai, *Nanoscale Advances in Catalysis and Energy Applications.* Nano Letters, 2010. **10**(7): p. 2289-2295.
5. Niemantsverdriet, J.W., et al., *Realistic surface science models of industrial catalysts.* Applied Surface Science, 1999. **144-145**: p. 366-374.
6. Iwasa, N., et al., *STEAM REFORMING OF METHANOL OVER PD/ZNO - EFFECT OF THE FORMATION OF PDZN ALLOYS UPON THE REACTION.* Applied Catalysis a-General, 1995. **125**(1): p. 145-157.
7. Studt, F., et al., *Identification of non-precious metal alloy catalysts for selective hydrogenation of acetylene.* Science, 2008. **320**(5881): p. 1320-1322.
8. Van Santen, R.A., et al., *Catalysis: An Integrated Approach*. 2000: Elsevier.
9. Li, Y. and G.A. Somorjai, *Nanoscale Advances in Catalysis and Energy Applications.* Nano Letters, 2010. **10**(7): p. 2289-2295.
10. Rodriguez, J.A., *Interactions in Bimetallic Bonding: Electronic and Chemical Properties of PdZn Surfaces.* The Journal of Physical Chemistry, 1994. **98**(22): p. 5758-5764.
11. Rodriguez, J.A. and D.W. Goodman, *The Nature of the Metal-Metal Bond in Bimetallic Surfaces.* Science, 1992. **257**(5072): p. 897-903.
12. Kovnir, K., et al., *A new approach to well-defined, stable and site-isolated catalysts.* Science and Technology of Advanced Materials, 2007. **8**(5): p. 420-427.
13. Karim, A., T. Conant, and A. Datye, *The role of PdZn alloy formation and particle size on the selectivity for steam reforming of methanol.* Journal of Catalysis, 2006. **243**(2): p. 420-427.
14. Lin, S., D.Q. Xie, and H. Guo, *Pathways of Methanol Steam Reforming on PdZn and Comparison with Cu.* Journal of Physical Chemistry C, 2011. **115**(42): p. 20583-20589.
15. Boudart, M., *Turnover Rates in Heterogeneous Catalysis.* Chemical Reviews, 1995. **95**(3): p. 661-666.
16. Musselwhite, N. and G. Somorjai, *Investigations of Structure Sensitivity in Heterogeneous Catalysis: From Single Crystals to Monodisperse Nanoparticles.* Topics in Catalysis, 2013. **56**(15-17): p. 1277-1283.
17. Neyman, K.M., et al., *Microscopic models of PdZn alloy catalysts: structure and reactivity in methanol decomposition.* Physical Chemistry Chemical Physics, 2007. **9**(27): p. 3470-3482.
18. Halevi, B., et al., *Aerosol-Derived Bimetallic Alloy Powders: Bridging the Gap.* Journal of Physical Chemistry C, 2010. **114**(40): p. 17181-17190.

19. Conant, T., et al., *Stability of bimetallic Pd-Zn catalysts for the steam reforming of methanol.* Journal of Catalysis, 2008. **257**(1): p. 64-70.
20. Friedrich, M., et al., *High CO2 Selectivity in Methanol Steam Reforming through ZnPd/ZnO Teamwork.* Angewandte Chemie International Edition, 2013. **52**(16): p. 4389-4392.
21. Iwasa, N., et al., *Selective PdZn alloy formation in the reduction of Pd/ZnO catalysts.* Bulletin of the Chemical Society of Japan, 1998. **71**(6): p. 1451-1455.
22. Dagle, R., Y.-H. Chin, and Y. Wang, *The Effects of PdZn Crystallite Size on Methanol Steam Reforming.* Topics in Catalysis, 2007. **46**(3): p. 358-362.
23. Penner, S., et al., *Growth and structural stability of well-ordered PdZn alloy nanoparticles.* Journal of Catalysis, 2006. **241**(1): p. 14-19.
24. Gunter, P.L.J., et al., *Surface Science Approach to Modeling Supported Catalysts.* Catalysis Reviews, 1997. **39**(1-2): p. 77-168.
25. Kuipers, E.W., C. Laszlo, and W. Wieldraaijer, *Deposition of nanocrystals on flat supports by spin-coating.* Catalysis Letters, 1993. **17**(1): p. 71-79.
26. Vanhardeveld, R.M., et al., *DEPOSITION OF INORGANIC SALTS FROM SOLUTION ON FLAT SUBSTRATES BY SPIN-COATING - THEORY, QUANTIFICATION AND APPLICATION TO MODEL CATALYSTS.* Applied Surface Science, 1995. **84**(4): p. 339-346.
27. van den Oetelaar, L.C.A., et al., *A surface science study of model catalysts. 1. Quantitative surface analysis of wet-chemically prepared Cu/SiO2 model catalysts.* Journal of Physical Chemistry B, 1998. **102**(47): p. 9532-9540.
28. Peterson, E.J., et al., *Aerosol synthesis and Rietveld analysis of tetragonal (beta(1)) PdZn.* Journal of Alloys and Compounds, 2011. **509**(5): p. 1463-1470.
29. Nesic, S. and J. Vodnik, *KINETICS OF DROPLET EVAPORATION.* Chemical Engineering Science, 1991. **46**(2): p. 527-537.
30. David Williams, C.B.C., *Transmission Electron Microscopy: A Textbook for Materials Science* 2ed. 2009, New York Springer. 760.
31. Datye, A.K., *Handbook of Heterogenous Catalysis* 1ed. Characterization of Solid Catalysts ed. H.K. G. Ertl, J. Weitkamp. Vol. 2. 1997, Weinheim: VCH Verlagsgesellschaft mbH. 4270.
32. Niemantsverdriet, J.W., *Microscopy and Imaging*, in *Spectroscopy in Catalysis*. 2007, Wiley-VCH Verlag GmbH & Co. KGaA. p. 179-216.
33. Crewe, A.V., *Scanning Electron Microscopes: Is High Resolution Possible?* Science, 1966. **154**(3750): p. 729-738.
34. Crewe, A.V., J. Wall, and L.M. Welter, *A High,ÄêResolution Scanning Transmission Electron Microscope.* Journal of Applied Physics, 1968. **39**(13): p. 5861-5868.
35. Pennycook, S.J. and P.D. Nellist, *Scanning Transmission Electron Microscopy: Imaging and Analysis*. 2011: Springer.
36. Delannay, F., *Characterization of heterogeneous catalysts*. 1984: M. Dekker.
37. Borgna, A., et al., *Pt-CO/SiO2 bimetallic planar model catalysts for selective hydrogenation of crotonaldehyde.* Journal of Physical Chemistry B, 2004. **108**(46): p. 17905-17914.
38. Griswold, E., A. Ash, and L. McReynolds, *The Solvent Effect of Lithium Nitrate on Zinc Acetate in Acetic Acid.* Journal of the American Chemical Society, 1945. **67**(3): p. 372-374.

39. Burton, P.D., T.J. Boyle, and A.K. Datye, *Facile, surfactant-free synthesis of Pd nanoparticles for heterogeneous catalysts.* Journal of Catalysis, 2011. **280**(2): p. 145-149.
40. Massalski, T.B., H. Okamoto, and A.S.M. International, *Binary alloy phase diagrams*. 1990, Materials Park, Ohio: ASM International.
41. McBride, J.R., K.C. Hass, and W.H. Weber, *Resonance-Raman and lattice-dynamics studies of single-crystal PdO.* Physical Review B, 1991. **44**(10): p. 5016-5028.
42. Xing, L.L., et al., *High gas sensing performance of one-step-synthesized Pd-ZnO nanoflowers due to surface reactions and modifications.* Nanotechnology, 2011. **22**(21).
43. FoÃàttinger, K., et al., *Dynamic Structure of a Working Methanol Steam Reforming Catalyst: In Situ Quick-EXAFS on Pd/ZnO Nanoparticles.* The Journal of Physical Chemistry Letters, 2011. **2**(5): p. 428-433.
44. Uemura, Y., et al., *Formation and oxidation mechanisms of Pd-Zn nanoparticles on a ZnO supported Pd catalyst studied by in situ time-resolved QXAFS and DXAFS.* Physical Chemistry Chemical Physics, 2012. **14**(7): p. 2152-2158.
45. Chen, M. and L.D. Schmidt, *Morphology and sintering of platinum crystallites on amorphous silicon dioxide.* J. Catal., 1978. **55**(3): p. 348-60.
46. Penner, S., et al., *Growth and structural stability of well-ordered PdZn alloy nanoparticles.* Journal of Catalysis, 2006. **241**(1): p. 14-19.
47. Th¸ne, P.C. and J.W. Niemantsverdriet, *Surface science models of industrial catalysts.* Surface Science, 2009. **603**(10-12): p. 1756-1762.
48. Moodley, P., et al., *Is there a correlation between catalyst particle size and CNT diameter?* Carbon, 2009. **47**(8): p. 2002-2013.
49. De Ruijter, W., et al., *Quantification of high-resolution lattice images and electron holograms.* SCANNING MICROSCOPY-SUPPLEMENT-, 1992: p. 347-347.
50. Boudias, C., *CaRIne Crystallography Software 3.1*. 1989-2005. p. The crystallographic software for research and teaching.
51. Vizdal, J., et al., *The Experimental and Theoretical Study of Phase Equilibria in the Pd–Zn (-Sn) System.* Advanced Engineering Materials, 2006. **8**(3): p. 164-176.
52. Assadi, M.H.N., et al., *Structural and electronic properties of Eu- and Pd-doped ZnO.* Nanoscale Research Letters, 2011. **6**.
53. Cubeiro, M.L. and J.L.G. Fierro, *Selective production of hydrogen by partial oxidation of methanol over ZnO-Supported palladium catalysts.* Journal of Catalysis, 1998. **179**(1): p. 150-162.
54. Iwasa, N. and N. Takezawa, *New Supported Pd and Pt Alloy Catalysts for Steam Reforming and Dehydrogenation of Methanol.* Topics in Catalysis, 2003. **22**(3-4): p. 215-224.
55. Tamaru, K., *Dynamic heterogeneous catalysis*. 1978: Academic Press.
56. Iwasa, N., et al., *Steam reforming of methanol over Pd-Zn catalysts.* Reaction Kinetics and Catalysis Letters, 2000. **69**(2): p. 355-360.
57. Freund, H.-J., et al., *CO Oxidation as a Prototypical Reaction for Heterogeneous Processes.* Angewandte Chemie International Edition, 2011. **50**(43): p. 10064-10094.
58. Johnson, R.S., et al., *The CO oxidation mechanism and reactivity on PdZn alloys.* Physical Chemistry Chemical Physics, 2013. **15**(20): p. 7768-7776.
59. Vajtai, R., *Springer Handbook of Nanomaterials*. 2013: Springer.